NANO · MICRO small
www.small-journal.com

Single-Atom Catalysts Derived from Metal–Organic Frameworks for Electrochemical Applications

*Lianli Zou, Yong-Sheng Wei, Chun-Chao Hou, Caixia Li, and Qiang Xu**

Single-atom catalysts (SACs) have received tremendous attention due to their extraordinary catalytic performances. The synthesis of this kind of catalysts is highly desired and challenging. In the last few years, metal–organic frameworks (MOFs) have been demonstrated as a promising precursor for fabricating SACs. In this review, the progress and recent advances in the synthesis of MOF-derived SACs and their electrochemical applications are summarized. First, the synthetic approaches based on MOFs and accessible characterization techniques for SACs as well as their advantages/disadvantages are discussed. Then, the electrochemical applications of these MOF-derived SACs including the oxygen reduction reaction (ORR), oxygen evolution reaction (OER), hydrogen evolution reaction (HER), CO_2 reduction reaction (CO_2RR), nitrogen reduction reaction (NRR), and other energy-related reactions are reviewed. Finally, insights into the current challenges and future prospects of this field are briefly presented.

1. Introduction

Heterogeneous catalysts have received tremendous attention in fields of chemistry, energy, environmental protection, and so on.[1] As a kind of classical heterogeneous catalysts, metal nanoparticles (NPs) immobilized on various supports are very important for the energy storage and conversion.[2] The catalytic performances of metal NPs are highly dependent on the size of metal particles decorated on supports, which usually consist of hundreds of metal atoms with a wide size distribution. These different sizes of metal NPs might have multiple active sites that show a relatively low selectivity in a specific reaction, and thus affect the utilization of metal atoms.[3] To obtain a high-performance catalyst, enormous efforts have been devoted to this research area, such as choosing a proper support, optimizing the metal contents, and decreasing the geometric size of NP.[4] In a word, the aims of these strategies are based on improving the active sites and maximizing the utilization of metals. Recent researches have shown that reducing the metal NPs is regarded as a promising approach to largely improve catalytic performances with enhanced activities and selectivities, which will reach the maximum value when downsizing the metal NPs into isolated metal atoms.[5]

Single-atom catalysts (SACs) with individual active sites dispersed on functional supports, emerging as a new frontier in catalysis and materials science, have become one of the hottest research topics in recent years. These active sites are actually heteroatoms including metal-, semimetal-, and nonmetal-atoms decorated on various supports.[6] Due to their superior catalytic performances, metal-based SACs, the only focus of this review, have been receiving more and more attention. Compared to traditional heterogeneous metal NP catalysts, SACs can not only exhibit the advantages of homogeneous catalysts with boosting catalytic activity and ultrahigh selectivity, but also inherit the unique characteristics of heterogeneous catalysts such as excellent stability and easy separation and recycling, which show great potentials to bridge the gap between homogeneous and heterogeneous catalysts.[5a,6b,7] In 1991, Basset and co-workers reported a kind of discrete zirconium hydride supported on silica for heterogeneous catalysis.[8] Then, Thomas and co-workers reported a titanium-related heterogeneous catalyst by grafting metallocene complexes onto the inner walls of mesoporous SiO_2 in 1995.[9] Following, Heiz and co-workers studied the catalytic performance of Pd_n clusters ($1 \leq n \leq 30$) on MgO for acetylene cyclotrimerization in 2000, and found that the benzene could be formed on a single palladium atom at a low temperature (300 K).[10] In 2001, Kobayashi studied the activity and selectivity of isolated site or mononuclear structure of metals on silica-based supports, which showed a higher turnover frequency (TOF) than cluster catalysts.[11] Lee and co-workers prepared the single-site mesoporous Pd/Al_2O_3 catalysts in 2007, showing a very high activity for aerobic oxidation, and they also found that Pd atoms supported on Al_2O_3 were mobile under electron beam.[12] In 2011, Zhang and co-workers reported the SACs by depositing single Pt atoms on iron oxides, which exhibited the high activity and stability for CO oxidation.[13] In 2016, Li's group reported the synthesis of SACs with a metal loading up to 4 wt% using MOF as precursors.[14] Up to now, a variety of synthetic strategies have been developed for the synthesis of single-, dual-atom catalysts, which showed a great potential in energy-related applications.[15]

Owing to their tunable electronic structure and low-coordinated configuration, SACs have displayed attractive

Dr. L. Zou, Dr. Y.-S. Wei, Dr. C.-C. Hou, Dr. C. Li, Prof. Q. Xu
AIST-Kyoto University Chemical Energy Materials Open Innovation Laboratory (ChEM-OIL)
National Institute of Advanced Industrial Science and Technology (AIST)
Yoshida, Sakyo-ku, Kyoto 606-8501, Japan
E-mail: q.xu@aist.go.jp
Prof. Q. Xu
School of Chemistry and Chemical Engineering
Yangzhou University
Yangzhou, Jiangsu 225009, P. R. China
E-mail: qxuchem@yzu.edu.cn
The ORCID identification number(s) for the author(s) of this article can be found under https://doi.org/10.1002/smll.202004809.

DOI: 10.1002/smll.202004809

applications in electrochemical energy conversion and storage, such as oxygen reduction reaction (ORR),[16] oxygen evolution reaction (OER),[17] hydrogen evolution reaction (HER),[18] carbon dioxide reduction reaction (CO_2RR),[19] and nitrogen reduction reaction (NRR).[20] Because these SACs are generally single-metal atoms decorated on metal oxide,[21] nitride,[22]or carbon,[23] the supports are of significant importance for their chemical properties. To achieve atomically dispersed separation and isolation of atoms and to prevent the as-formed single atoms from migration and agglomeration, a variety of synthetic strategies have been reported for the development of SACs, such as pyrolysis,[24] wet chemistry synthesis,[25] physical and chemical vapor deposition,[26] electrochemical deposition,[27] photoreduction process,[21] and so on. To date, many noble or non-noble metal-based SACs, such as Pt,[28] Pd,[21,28a] Au,[29] Ru,[30] Zn,[31] Fe,[32] Co,[33] Ni,[34] Mn,[16a,35] Cu,[19c,36] etc., have been synthesized through the above mentioned approaches. However, fabricating SACs and maintaining the metal centers as atomically dispersed sites under both synthesis and catalysis conditions are challenging. The sharply increased surface free energy at an atomic level will lead to the aggregation of atoms automatically during the synthesis and application, if the loading of metals is too high. Thus, most of SACs suffer from a very low amount of metal loading, which is usually lower than 3 wt% to prevent the tendency of aggregation.[22c,37] Finding a proper precursor that can achieve high specific surface areas of supports and enhance the loading of metals is useful for the preparation of high-performance SACs.

Metal–organic frameworks (MOFs), also called porous coordination polymers (PCPs), a new class of porous crystalline materials that construct by the coordinating inorganic nodes (metal ions/clusters) and organic ligands, have been extensively studied in various applications since the 1990s.[38] Attributed to their unique advantages of ultrahigh surface areas, well-defined pore structures, and adjustable compositions and functionalities, MOFs show great potentials in fields of gas storage and separation,[39] catalysis,[40] energy storage, and so on.[41] In the past decades, MOFs have widely been used as precursors for the preparation of functional nanomaterials like metal oxides,[41b,42] porous carbons,[43] nitrides,[44] phosphides,[45] or their composites.[46] Because of the atomically dispersed metal sites separated by organic linkers, MOFs are exactly SACs, which can be further used as self-sacrificed precursors/templates to prepare stable MOF-derived SACs.[17,47] Attributed to MOFs having advantages in following aspects, such as various kinds of organic linkers with functional groups, uniform distributed metal clusters for exchanging, unsaturated metal sites for coordination, and ordered pore structures that benefit for the adsorption of small molecules, MOFs are an ideal platform for immobilizing desired metal species. Through a simple pyrolysis process, single-metal atoms supported on carbons can be easily achieved from MOFs or MOF composites. For example, the carbonization of MOFs with N-containing species results in the formation of nitrogen-doped porous carbon materials, providing abundant anchors for single-metal atoms immobilization and achieving the stable SACs.[48] Usually, using MOFs as precursors for MOF-derived SACs enhance not only the metal loading of catalysts but also the stability of SACs, which attract tremendous interest in the field of electrochemical energy conversion.

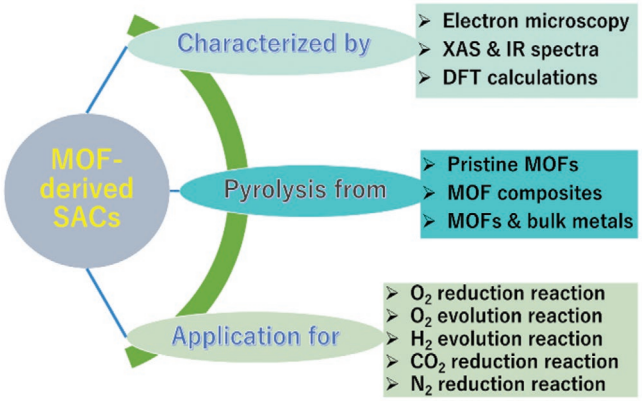

Figure 1. Schematic illustration of MOF-derived SACs including the synthesis strategies, characterization techniques, and various electrochemical applications.

Although the MOF-derived SACs have just been studied in a few years, the sharply increasing researches on this field indicated the great advantages of SACs deriving from MOFs and demonstrated their promising potentials in energy-related aspects, opening a new chapter between MOFs and SACs. This timely review aims to afford readers with a deep insight into the development of MOF-derived SACs and explore their potential applications in fields of energy and chemistry. In following sections, we will discuss the syntheses and characterizations of MOF-derived SACs and summarize their electrochemical applications (**Figure 1**). At the end of this review, the future outlooks and our viewpoints on this emerging research topic are presented. We hope our work can promote more significant breakthroughs in the development of MOF-derived SACs.

2. Synthetic Strategies for SACs from MOFs

It should be noted that MOFs can be directly used as supports for single-metal atoms immobilization, which can be seen from previous reports.[28b,49] In this review, we will only focus on the SACs obtained from the carbonization of MOFs. To fabricate a uniform SAC, one of the key points is how to encapsulate the desired metal species into precursors. Comparing with other precursors, the synthesis of SACs from MOFs does not need a further dispersion of metal atoms, which just need a main pyrolysis step with a following evaporating or etching process. Those metal atoms separated by ligands in MOF structure will directly transform into target atoms after carbonization, giving a close contact between metal atoms and supports and thus achieving a superior stability during catalysis process. As we know, MOFs are constructed by ligands and metal nodes with ordered pore structures. These functional organic linkers can provide abundant coordination sites for the decoration of desired metal atoms, and the coordinatively unsaturated metal clusters can be furnished by coordinating other functional groups. What's more, the interconnected pores supply a proper space to accommodate various guest species that might convert into single-dispersed metal atoms after carbonization. Therefore, the MOF strategy makes it easier to design and tailor the

composition of SACs. Additionally, MOF-derived carbon supports usually show large surface areas and high pore volumes, which give a better dispersion of metal sites and facilitate the transport of mass during catalytic reactions. In this section, the synthetic approaches for MOF-derived SACs are introduced via the functionalization of linkers, metal species, or pores of MOFs.

2.1. Pyrolysis of Pristine MOFs

2.1.1. Single-Metal Strategy

Owing to that MOFs are constructed by metal atoms and organic ligands, SACs can be prepared by the direct pyrolysis of pristine MOFs. During the carbonization process, the organic ligands transform into carbon supports for immobilizing in situ reduced metal atoms. As a classical Zn-based MOF, ZIF-8 has been considered as a good precursor for preparing N-doped porous carbons owing to the high content of N on ligands.[4a,43b] It is demonstrated that the ZIF-8 is also a promising candidate for developing Zn SACs. By using ZIF-8 as the precursors, Jiang and co-workers reported a hollow porous carbon catalyst with uniform N active sites and an ultrahigh loading of Zn single atoms.[31] First, core–shell PS@ZIF composites (polystyrene (PS)) were synthesized by assembling ZIF-8 NPs on the surface of carboxylic acid modified PS NPs (**Figure 2**a). With a following removal of PS core in *N,N*-dimethyl formamide solution, spherical hollow ZIF-8 nanostructures showing a cavity size of 210 nm and shell thickness about 25 nm were obtained. Then, the hollow ZIF-8 spheres were pyrolyzed at different temperatures to form the hollow porous carbon decorated with Zn single atoms, and the samples obtained at 800 °C showed an extraordinarily high loading of Zn, as large as 11.3 wt%, much higher than the metal content in general SACs. Owing to its unique porous shell with abundant atomically dispersed Zn–N active sites, the synthesized Zn-SACs exhibited excellent catalytic activity in CO_2 cycloaddition with epoxides. Generally, Zn-based MOFs can transform into SACs via the one-step carbonization strategy owing to the relatively low evaporation temperature of metallic Zn (<950 °C), while other metal-based MOFs usually form carbon composites incorporated with metal NPs, which need a further acid treatment process to remove the metal NPs and result in SACs. Additionally, a secondary heating treatment is necessary for the acid leaching samples to repair the damaged carbon supports and improve the catalytic activity and structure stability. For example, using a Ni-MOF as the precursor, the Ni-SACs are obtained through the carbonization process, followed by the acid leaching and activation process.[50] As shown in Figure 2b, the Ni-MOF was first transformed into carbon composites with both Ni NPs and atomically dispersed Ni atoms, in which the Ni NPs could be removed through the acid leaching in HCl solution and a following electrochemical activation process under a constant potential. The prepared Ni-SACs showed a good catalytic performance for HER in acidic conditions. Through the carbonization of a Mn-1,3,5-benzenetricarboxylic acid (BTC) framework under N_2 flows with a following acid etching and NH_3 activation, Yang et al. developed a Mn-SAC by dispersing Mn single atoms on a 3D graphene-like carbon.[16a] In this strategy, ultrafine MnO NPs immobilized on carbon framework were removed in HCl solution, forming a porous structure, and the further annealing process in NH_3 flow facilitated the dispersion of Mn atoms on graphene. Different from the most of reported SACs, the obtained Mn-SAC showed a unique coordination structure with both N and O atoms coordinated on Mn centers. This research also demonstrates that besides N atoms, O atoms also play an important role for improving the activity of coordinated metal centers.

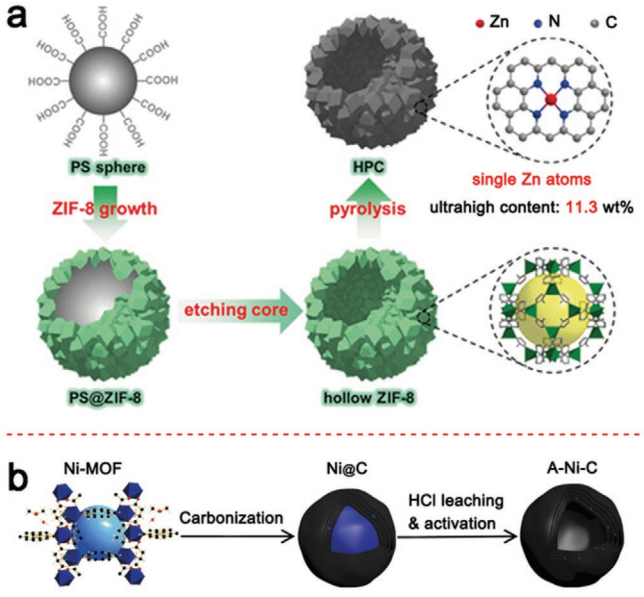

Figure 2. a) Synthesis of hollow porous carbon (HPC)-immobilized ultrahigh content of single Zn atoms. Reproduced with permission.[31] Copyright 2019, Wiley-VCH. b) Synthesis of Ni-SACs by the direct carbonization of Ni-MOF with a following etching and activation process. Reproduced with permission.[50] Copyright 2016, Nature Publishing Group.

2.1.2. Mixed-Metal Strategy

The metal nodes in MOFs can be easily replaced by other metal species, which provide a facile process to disperse target metal atoms in MOF structure. To date, the mostly used MOF precursors for SACs are Zn-based bimetallic MOFs, in which the Zn species can be removed by the self-evaporation process during the pyrolysis, while the other kind of metal atoms will be reduced and isolatedly distributed on the in situ generated carbons. As far as we know, the nitrogen-rich ZIF-8 is considered as a promising sacrificial precursor for this strategy. Via the one-pot approach or post-treatment process based on ion-exchange mechanism, the Zn centers can be replaced by other bivalent or even trivalent metal ions with a similar size, such as Fe^{2+}, Co^{2+}, Ni^{2+}, etc., forming a bimetallic ZIF structure with highly dispersed target metal atoms. During the carbonization process, the N-containing ligands will transform into N-doped carbon for anchoring and stabilizing the isolated target atoms, and the evaporating Zn species at high temperatures results in the formation of porous carbon supports that benefit the transportation of mass during catalysis process. For example, a

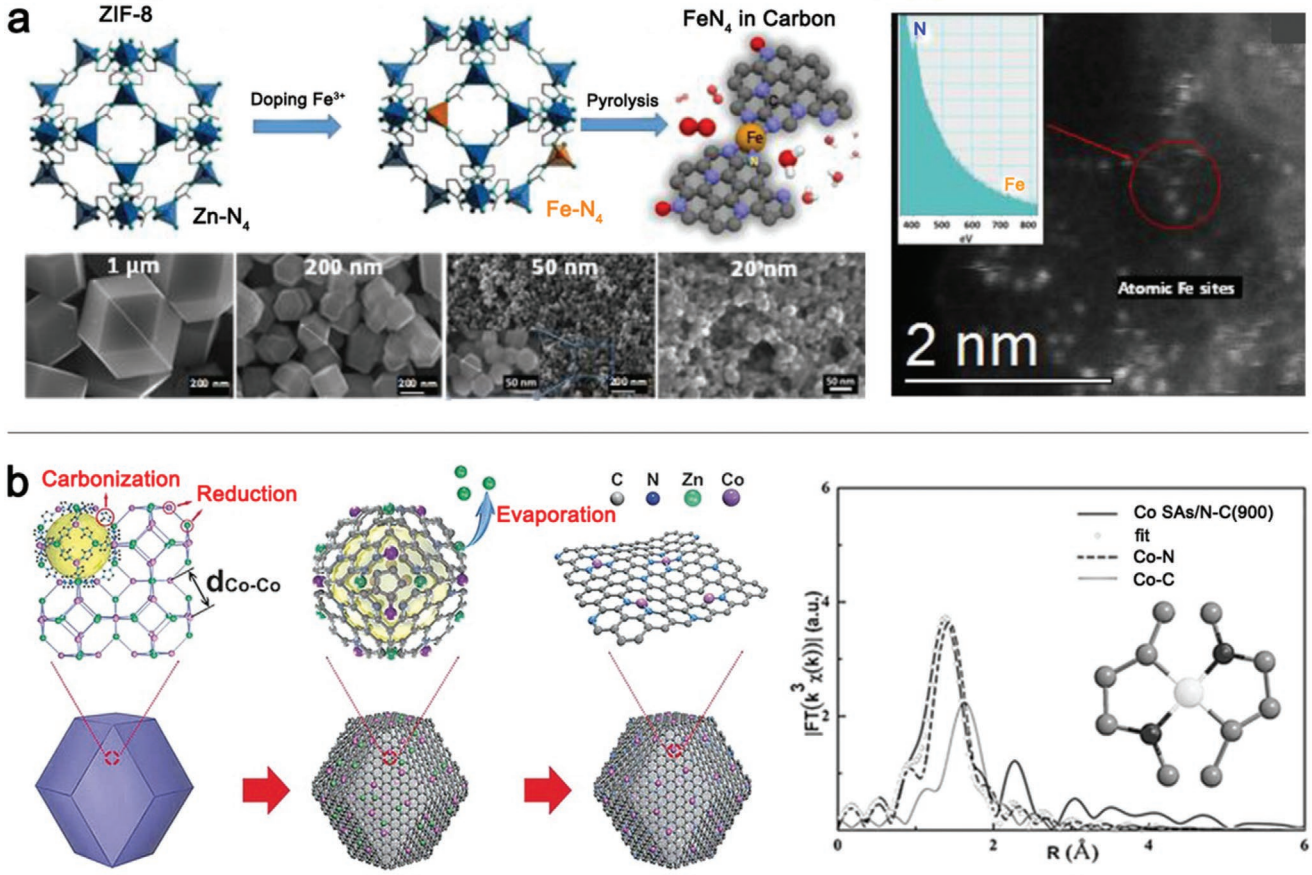

Figure 3. Construction of MOF-derived SACs by the mixed-metal strategy. a) Synthesis illustration of the Fe single-atom catalysts derived from different sizes of Fe-doped ZIFs and the inset shows the EELS results. Reproduced with permission.[51] Copyright 2017, American Chemical Society. b) The synthesis process and calculated structure of Co SAs/N–C fabricated by the carbonization of Co-doped ZIF-8. Reproduced with permission.[14] Copyright 2016, Wiley-VCH.

high-performance porous carbon supported with Fe–N_4 species was synthesized via the one-step thermal transformation of Fe-doped ZIF-8 nanostructures (**Figure 3**a).[51] By using Fe^{3+} ions as the doping metals, Zn–N_4 groups were successfully replaced by Fe–N_4 in ZIF-8. After being pyrolyzed at high temperatures, atomic Fe sites immobilized on carbons derived from ZIFs with different particle sizes ranging from 20 to 1000 nm were fabricated, and their ORR catalytic performances were significantly dependent on particle sizes of catalysts. Apart from Fe species, Co single atoms loaded on N-doped carbon catalysts can also be prepared by carbonizing Co-doped ZIF-8.[33b,52] Yin et al. synthesized a Co-SAC via the one-step pyrolysis of bimetallic Zn/Co-ZIF with highly distributed Zn^{2+} and Co^{2+} ions in the framework (Figure 3b). The Zn and Co cations were reduced to metallic Zn and Co during the decomposition of organic linkers, while the Zn atoms were evaporated above the boiling point, resulting in the formation of single Co atoms anchoring on N sites. The coordinating modes of Co species are highly related to carbonization temperatures. The samples obtained at 800 and 900 °C displayed the structure of Co–N_4 and Co–N_2, respectively, and the Co–N_2 sites showed a superior ORR electrocatalytic activity to Co–N_4 species. To disperse target metal ions in MOF precursors, the ion-exchange process is another efficient approach.[53] Through the ionic-exchange process between Zn metal nodes in ZIF-8 and Ni ions in solvents, Ni SAs homogeneously distributed in the whole carbon framework have been obtained by the pyrolysis of samples in argon atmosphere.[53b]

2.1.3. Metal-Containing Ligand Strategy

Because MOFs are assembled by metal nodes and organic linkers, the organic linkers can be functionalized by incorporating with heteroatoms. To prepare a desired single-metal atom catalyst, decorating target metals on organic ligands in MOF structure is another effective strategy to disperse metal atoms in precursors, and thus facilitating the formation of isolated metal atoms on carbon supports. Taking porphyrin as an example, the Zr-based MOF precursors with Fe doping were synthesized by using 80% H_2-TCPP (TCPP = tetrakis(4-carboxyphenyl)porphyrin) and 20% Fe-TCPP as ligands (**Figure 4**a), in which the distance of Fe center was enlarged by the large amount of H_2-TCPP in MOFs.[54] After carbonization in an inert atmosphere with a following acid etching process, Fe single atoms dispersed on N-doped porous carbons (Fe_{SA}–N–C) were obtained. The

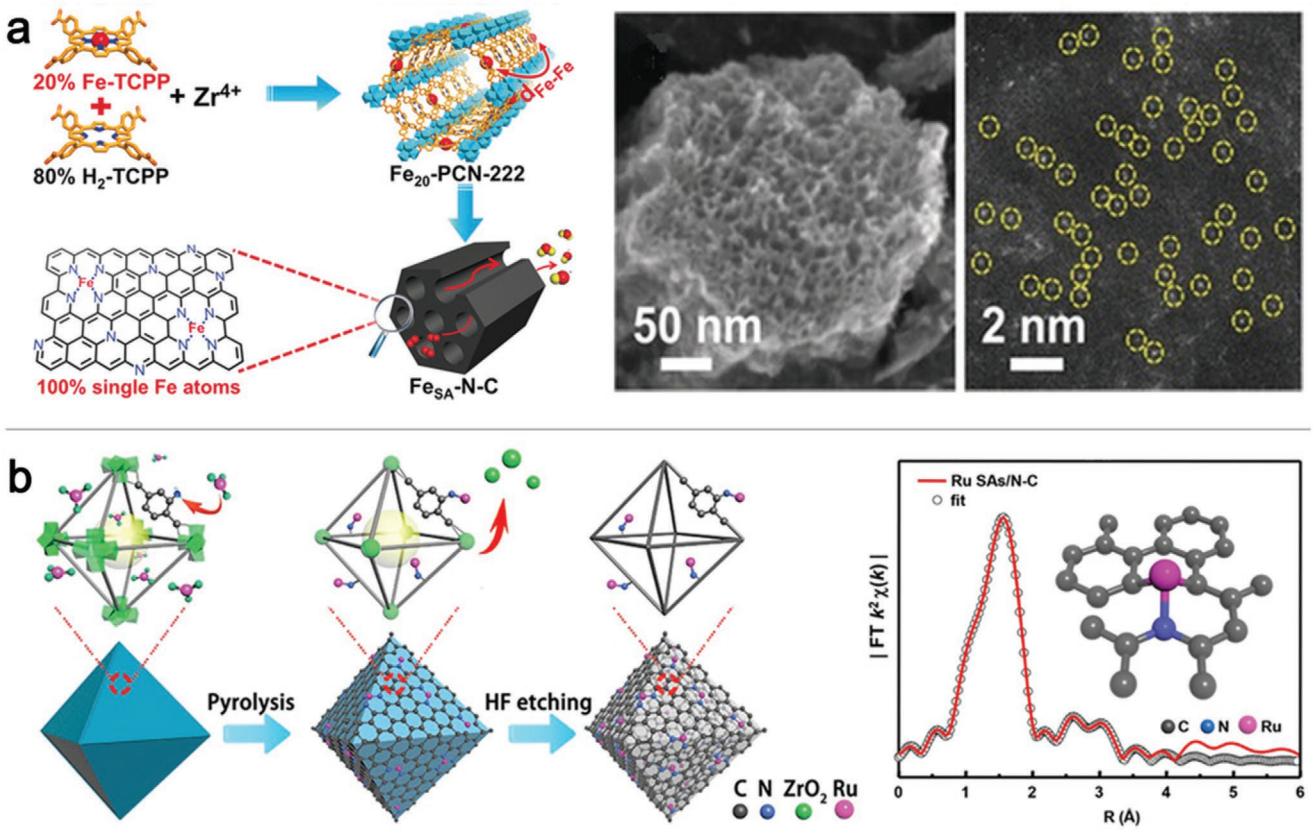

Figure 4. Construction of MOF-derived SACs by the metal-containing ligand strategy. a) Schematic illustration and electronic images of the Fe_{SA}–N–C. Reproduced with permission.[54] Copyright 2018, Wiley-VCH. b) Scheme of the proposed formation mechanism for Ru SAs by pyrolysis of MOFs and the proposed coordination structure. Reproduced with permission.[30] Copyright 2017, American Chemical Society.

scanning electron microscopy (SEM) analysis confirmed the highly ordered mesoporous structure of the resulting products, and isolated Fe atoms on carbons could be directly observed from high-angle annular dark-field imaging-scanning transmission electron microscope (HAADF-STEM) images. Fitting results of extended X-ray absorption fine structure (EXAFS) data demonstrated the formation of Fe–N_4 configuration of the catalysts, which showed excellent catalytic performance for ORR in both acid and alkaline conditions. In 0.1 M KOH solution, a half-wave potential of 0.891 V (reversible hydrogen electrode (RHE)) was achieved, much higher than Pt/C catalysts and samples prepared from MOF-derived carbons. Up to now, most of the single-metal atoms immobilized on carbon supports are connected through the N defects in carbon framework, which suggests the important roles of N species in MOF-derived SACs. Thus, to improve the distribution of metal sites as well as their stabilities, introducing N-related groups on linkers is a promising method for synthesizing SACs. In 2017, Li and co-workers reported a Ru SA/N–C catalyst via the coordination-assisted method, which was based on the utilization of strong coordination between the Ru^{3+} and free $-NH_2$ groups located on terephthalic acid linkers within MOFs.[30] As shown in Figure 4b, uncoordinated $-NH_2$ on linkers are used as the Lewis base to stabilize single Ru metal atoms and prevent their aggregations during the calcination process at high temperatures. After removing ZrO_2 in hydrogen fluoride (HF) solution, octahedral shaped Ru SAs/N–C catalysts retaining the morphology of UiO-66-NH_2 have been obtained. From the X-ray absorption near-edge spectroscopy (XANES) spectra and fitting results, Ru atoms are coordinated with two carbon atoms and one nitrogen atom, showing an average valence state of 3+. In control, without the assistance of $-NH_2$ groups, a large part of Ru atoms will aggregate into Ru NPs during the pyrolysis process. Taking the advantage of this strategy, W-SACs with N doping have been prepared through a similar process, which exhibit good catalytic performances for electrochemical hydrogen evolution.[55]

2.2. Pyrolysis of MOF Composites

2.2.1. Encapsulation of Metal Precursors within MOF Pores

One of the key attractions of MOFs is the adjustable porous structure, which is a promising host to encapsulate various functional guests. Thus, the utilization of these well-defined pores in MOFs to confine the metal atoms and prevent their aggregations during pyrolysis is another efficient approach for SACs derived from MOFs. To encapsulate metal atoms into pores of MOFs with uniform distributions, the double solvents methods (DSMs), which usually depend on the mixture solvents with a hydrophilic solvent and a hydrophobic solvent, are demonstrated to be convenient and effective. In 2017, Zhu et al. developed a kind of N-doped hierarchical graphitic

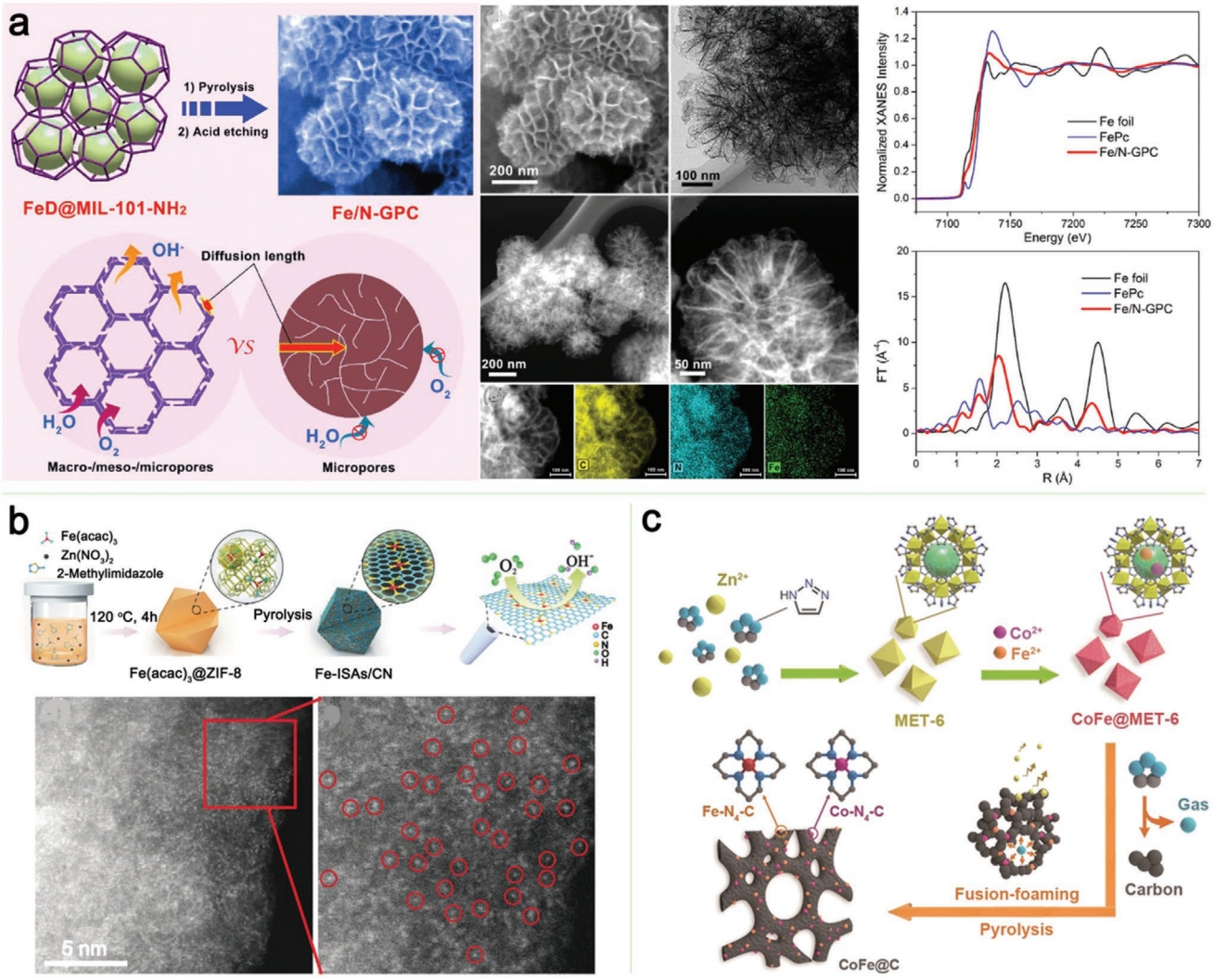

Figure 5. Fabrication of MOF-derived SACs via the pore confinement strategy. a) Schematic representation and characterization results of Fe/N-GPC catalysts via the pyrolysis of MIL-101-NH_2 absorbed Fe guests in the pores. Reproduced with permission.[48] Copyright 2017, American Chemical Society. b) Schematic illustration for the formation of Fe-ISAs/CN and corresponding TEM images. Reproduced with permission.[52] Copyright 2017, Wiley-VCH. c) Schematic illustration for the preparation of submillimeter-scale CoFe@C through the thermal treatment of CoFe-doped MET-6 particles. Reproduced with permission.[17] Copyright 2019, Wiley-VCH.

porous carbon architectures with highly dispersed Fe sites (**Figure 5**a).[48] Using MIL-101-NH_2 as a host MOF, the guest species of dicyandiamide (DCD) and Fe^{3+} were encapsulated into pores of MOFs by the DSM. The obtained MOF composites were then pyrolyzed under an argon flow and with a subsequent acid treatment, affording the graphitic porous carbon decorated with Fe, N active sites. XANES results suggested the formation of Fe–N_4 configurations in the catalyst. Such unique structures possessing hierarchical pores and high-density accessible metal centers showed good catalytic performances for ORR. It should be mentioned that the above DSM can be used for developing other kinds of metal SACs with controllable compositions by changing the guest species and avoiding the deposition of target metal atoms on the out surface of MOFs, which provides a facile strategy for synthesizing high-performance SACs with controllability. However, this method cannot encapsulate metal clusters with sizes larger than the windows of MOFs. Thus, strategies based on the in situ immobilization of metal species in MOF pores are developed.[52,56] As shown in Figure 5b, Chen et al. synthesized a Fe-SAC via a cage-encapsulated-precursor pyrolysis strategy. The ZIF-8 with a cavity diameter of 1.16 nm can be used as molecular-scale cages to encapsulate $Fe(acac)_3$ with the molecular diameter of 0.97 nm. One cavity can only trap one Fe-related molecular owing to the spatial confinement, and which cannot move to other cavities in MOFs attributing to the small window size of ZIF-8 (about 0.34), resulting in the formation of highly dispersed Fe species in ZIF nanostructures. After pyrolysis at 900 °C in argon flow, N-doped porous carbons were formed by the decomposition of 2-methylimidazole. Meanwhile, Fe ions in the cavities were reduced to isolated Fe single atoms anchoring on N atoms (Fe-ISAs/CN). The coupled plasma optical emission spectrometry (ICP-OES) demonstrated that the as-synthesized catalysts had a Fe content of 2.16 wt%. The highly accessible Fe-sites on N-doped carbons endowed the

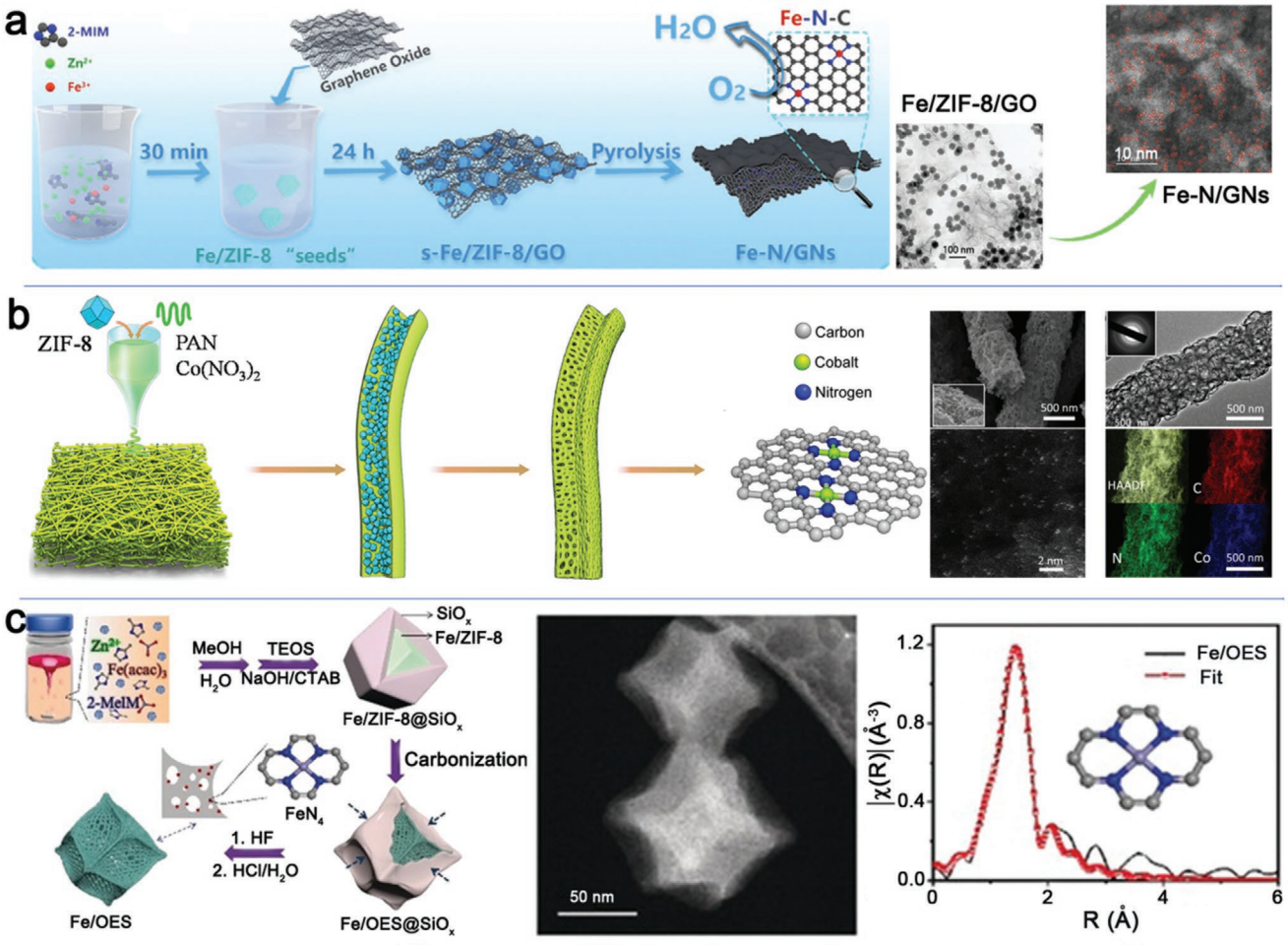

Figure 6. Fabrication of SACs by carbonizing composites of MOFs and functional materials. a) Synthesis of Fe–N/graphene nanosheets via the carbonization of ZIF/GO hybrids. Reproduced with permission.[24] Copyright 2020, Wiley-VCH. b) Presentation of the synthesis process and TEM images for CoSA/HCNFs from the composites of ZIF nanofibers. Reproduced with permission.[19b] Copyright 2020, Elsevier Ltd. c) Synthesis of Fe/OES with controlled structures by pyrolysis of core–shelled Fe/ZIF-8@SiO_x composites. Reproduced with permission.[7a] Copyright 2020, Wiley-VCH.

Fe-ISAs/CN with excellent performances for ORR, showing a half-wave potential of 0.9 V and a good methanol tolerance and outstanding stability. Apart from the single metals, two or more kinds of metal species isolatedly distributed on carbon supports can also be prepared by pyrolysis of MOF composites. Using the coimmobilization of Fe and Co atoms as an example, Zhao et al. reported the carbon-based SACs with isolated Co- and Fe-coordinated active sites (Figure 5c).[17] Taking the advantages of MOFs with well-defined pore structures, Fe and Co species were easily encapsulated into the pores of MET-6 (a zinc-coordinate triazole-rich energetic MOF), which could be reduced into single atoms dispersed on a submillimeter-sized N-doped carbon support after the evaporation of metallic Zn species under the high temperature. The hierarchical pores distributed from hundreds of nanometers to micrometers were strategically achieved during the pyrolysis process, attributed to the decomposition of energetic triazole ligands. The obtained Co–Fe@C catalysts with hierarchical pores, interconnected 3D structures and atomically dispersed Co and Fe sites exhibited an outstanding performance for ORR.

2.2.2. Composites of MOFs and Other Functional Materials

To control the morphology of MOF-derived SACs, combinating MOFs with other functional materials such as graphene, graphene oxides, or additional carbon and nitrogen sources is promising. In some cases, these addition materials not only contribute to morphology control but also enhance the utilization of single-metal sites. Lu et al. synthesized the Ni-SACs with Ni–N_4 structure by carbonizing hybrids of ZIF-8/DCD/Ni^{2+} (DCD stands for the dicyandiamide).[34b] The increased density of N sites on carbon supports during the decomposition of DCD was good for anchoring Ni single atoms. Liu et al. reported a ZIF-8 "thermal melting" strategy to fabricate 2D porous graphene nanosheets (GNs) with Fe and N doping (Fe–N/GNs).[24] During the pyrolysis, the Fe-doped ZIF-8 was thermally molten on graphene nanosheets, forming a thin N-doped porous carbon layer to capture Fe single atoms and increase the surface area of resulting catalysts (**Figure 6**a). The prepared Fe–N/GNs showed a high surface area of 1237.9 m^2 g^{-1} with abundant exposed Fe active

sites, exhibiting superb ORR activity in both alkaline and acidic electrolytes.

Aside from confining metal ions inside MOFs, using additional carbon sources to disperse and stabilize metal ions is another attractive approach. Via the addition of secondary carbon source, the metal species, morphologies, and compositions of final products can be efficiently controlled. Yang et al. fabricated a kind of Cu single atoms immobilized on interconnected porous carbon nanofiber by the carbonization of Cu-doped ZIF-8/PAN composites (polyacrylonitrile (PAN)).[57] They first synthesized Cu-ZIF-8/PAN composites via the electrospinning and then pyrolyzed these composites at 900 °C to get isolated Cu decorated on through-hole carbon nanofibers (CuSAs/TCNFs). The obtained CuSAs/TCNFs exhibited a honeycomb-like morphology with abundant of mesopores, which largely exposed Cu metal sites for the reduction of CO_2 to methanol. In addition, by the similar strategy, they fabricated a 3D net-like high-yield carbon membrane with single Co decorated (CoSA/HCNFs)[19b] or Ni immobilized (NiSA/PCFM).[19d] As shown in Figure 6b, using the electrospinning method, a 3D connected network composed of ZIF-8, Co^{2+}, and PAN is obtained, which transforms into Co-SACs with well-defined 3D structures after carbonization. The decomposition of PAN and ligands of ZIF-8 results in an interconnected carbon network with high-density of N defects for anchoring Co single atoms. It should be noted that ZIF-8 nanocrystals are vital to the formation of hierarchical pores in carbon nanofibers, which play an important role to enhance the mass transfer ability during catalysis process. Thus, the obtained CoSA/HCNFs exhibit an excellent performance for CO_2 electrochemical reductions.

During the thermal transformation of carbon-based precursors to SACs, N-defects are of vital importance for immobilizing single-metal atoms. When using non-nitrogen containing MOFs as precursors, an additional N source is necessary. The generally used N sources are DCD, melamine, and pyrroles. For example, Ni-SACs with different N coordination numbers have been synthesized by using a bimetallic MgNi-MOF-74 encapsulated with polypyrrole (PPy) as the precursor. The added Mg^{2+} in MOF structures can extend the distance between Ni atoms, facilitating the dispersion of Ni single atoms and preventing their aggregations, and the introduced PPy guests in 1D channels of MOFs serve as the N source to stabilize and capture Ni atoms. As a result, highly dispersed Ni singles atoms on a N-doped carbon support were achieved after carbonization with the following removal of MgO by etching. The metal content of these samples prepared at different temperatures was about 0.9 wt%.[58]

To enhance the surface areas and pore volumes of MOF-derived SACs, Hou et al. strategically developed an overhang-eave like carbon cage with isolated Fe single atoms (Fe/OES) for ORR,[7a] which showed a high utilization of Fe active sites with the surprisingly high TOF value of 25 S^{-1} (Figure 6c). The synthetic process for Fe/OES contained three steps: first, ZIF-8 was employed as a host to encapsulate $Fe(acac)_3$ molecular in pores; then, a thin layer of silicon oxide was deposited on the surface of ZIF-8 through a wet-chemistry method and formed a core–shell structure of Fe/ZIF-8@SiO_x; finally, the composites of Fe/ZIF-8@SiO_x were carbonized at the target temperature, followed by washing in HF and HCl solution to remove the SiO_x and finally resulting in the porous Fe/OES catalysts. In this strategy, the SiO_x layer is very important to the formation of overhang-eave like structure, which improves the catalytic activity during electrochemical reactions by providing more accessible active sites. Without SiO_x on the surface, the resulting carbon catalyst retains the original morphology of ZIFs and shows a much lower catalytic activity than Fe/OES samples. It has been proved that the SiO_2 in pores of MOFs can also improve the loading of single metals by dispersing the metal atoms, which results in a Fe content as high as 3.46 wt%.[59] Similarly, isolated Fe single atoms dispersed on a nitrogen, phosphorus and sulfur tridoped hollow carbon cages were fabricated by the pyrolysis of ZIF-8/Fe coating with cyclotriphospazene-*co*-4′4-sulfonyldiphenol (PZS).[32c] The decomposition of PZS during the calcination process led to the doping of P and N in carbons, enhancing the catalytic performances of this catalyst. In another example, He et al. developed a surfactant-assisted MOF approach to fabricate core–shell structured Co–N–C catalysts by using the surfactant of F127 polymer covered ZIF-8 nanostructure. The ZIF-8@F127 precursor-derived carbons showed a significantly increasing densities of active sites attributed to the confinement role of surfactants.[60]

2.3. Pyrolysis of MOFs with Bulk Metals: A Top-Down Strategy

Finding an economic and efficient strategy to synthesize SACs has attracted a great attention, and the transformation of bulk metals to single-metal atoms is considered as the feasible approach. The copyrolysis of MOFs with bulk metals via a thermal emitting process is another strategy for synthesizing SACs from MOF-based precursors. Wu and co-workers studied the conversion of Ni NPs into Ni-SACs by heating the composites of Ni NPs immobilized on N-containing carbon surface derived from ZIF-8,[34a] in which metal NPs are transformed into Ni single atoms through the thermal diffusion process. Under the high temperature, Ni NPs could break the C—C bonds and drill into the carbon matrix, which would form a strong N–Ni coordination when exposed to N defects, resulting in the formation of single Ni atoms immobilized on carbon frameworks. By contrast, in carbon supports without N-defects, Ni NPs cannot transform into single Ni atoms and only NPs with about 5 to 50 nm were observed, suggesting the vital importance of N anchors on carbons for the thermal transformation of metal NPs into single-metal sites. Taking the advantage of N-species that provide a strong coordination for metal atoms during the pyrolysis process, Li and co-workers synthesized a variety of noble-metal SACs by carbonizing M-NPs@ZIF-8 composites (M = Pt, Pd, Au).[61] Choosing Pd-SACs as the representative, the Pd-encapsulated ZIF-8 nanostructures were first synthesized by mixing $Zn(NO_3)_2$ and 2-MeIm with Pd NPs. As a result, ZIF-8 nanocrystals could grow around Pd NPs and form a Pd-NPs@ZIF-8 composite, which was used as the precursor for Pd-SACs via a thermal transformation process. With the increase of calcination temperatures, the agglomeration of Pd NPs into large-sized NPs was observed at the initial stage, while these enlarged Pd NPs would collapse and become smaller with the decomposition

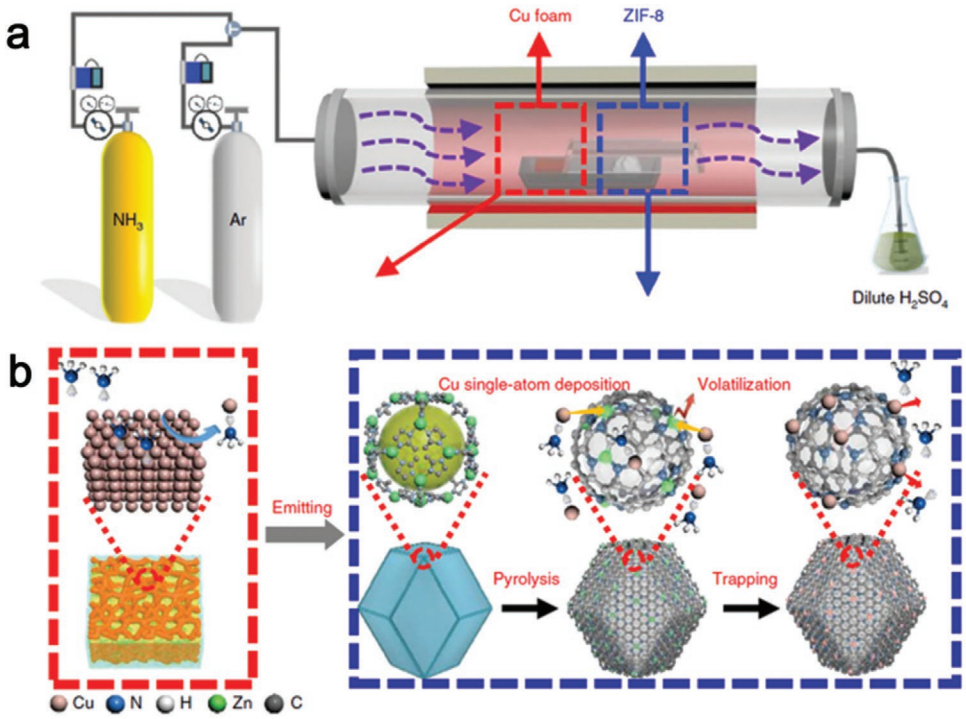

Figure 7. Synthesis of SACs by the copyrolysis of MOFs and metal salts under a high temperature. a) Apparatus diagram. b) Proposed reaction mechanism. Reproduced with permission.[26] Copyright 2018, Nature Publishing Group.

of ZIF-8. The ZIF-8-derived carbons provided abundant of N anchors for trapping mobile metal atoms from Pd NPs under the high temperatures, resulting in the decrease of metal NPs and finally forming the single atom dispersed carbon catalysts with a structure of M–N_4. Besides metal NPs on supports, the carbonization of bulk metals and MOFs in NH_3 atmosphere is a good choice for SACs (**Figure 7**).[26] Thus, they reported a facile thermal emission process to scalable synthesis of Cu-SACs by heating Cu foams and ZIF-8 powder in NH_3 flow. At 900 °C, the in situ produced carbons with high-density of N sites served as the ideal supports to capture $Cu(NH_3)_x$ species, leading to the formation of isolated Cu single atoms dispersed on porous carbon (CuSAs/N–C). This emission process is highly depended on the activation of NH_3 molecules under high temperatures, which coordinate with bulk Cu metals to form the mobile $Cu(NH_3)_x$ species that can be trapped by carbon supports. Without the NH_3 flow, Cu atoms will never be separated from Cu foams and deposited on ZIF-8-derived carbons. Thus, the movable metal species during thermal pyrolysis is very important for the formation of SACs. To further reveal the transformation process, the formation process of Fe–N_4 sites on carbon supports have been studied detailedly. It was demonstrated that Fe precursors were first transformed into FeO_x species at a relatively low temperature, which would convert into Fe–N_x species with the increase of calcination temperature because of the superior thermal stability of Fe–N_4 than Fe–O_4 groups in the existence of carbons under high temperatures. Even using different kinds of Fe precursors or via non-contact pyrolysis strategy, the similar transformation process has been observed.[32d] Of course, the pyrolysis temperature is another important factor that affects intrinsic properties of SACs. A proper heating temperature can increase the bonding strength and shorted length of Fe—N bonds, while a too high temperature often results in the loss of nitrogen and breaks the structure of Fe–N configurations.[32e]

Based on these progresses, it can be concluded that MOF-strategy is an effective approach for the synthesis of highly dispersed single-metal atoms supported on carbons. Among various methods for SACs from MOF precursors, the metal strategy and pore confinement strategy are widely used. Pyrolysis of MOFs with single-metal species usually resulting in the formation of single-metal atoms and metal NPs. Though it is simple, the removal of metal NPs is necessary, and the loading amount of metals are uncontrollable. Thus, mixed-metal strategies are more considerable and efficient, which also allow the formation of SACs with high loading of metals. However, this strategy can be just used for those MOFs in which metal species in pristine MOFs can be replaced or exchanged by target metals. As for the metal-containing ligand method, the lacking of relevant ligands for MOF production is the main barrier. Up to now, the available MOFs on this strategy are very rare. Theoretically, all kinds of metals can be confined in the pores of MOFs and transform into single-metal atoms after carbonization. Thus, pore confinement strategy has attracted great attention in the synthesis of SACs from MOF precursors. The biggest problem of this method lies in the loading of target metal species, which highly depend on the pore structure and pore volume of MOFs. It should be noted that most of present reports are focused on the Zn-related MOF precursors, in which the Zn species might evaporate with the gas flow under high temperatures and prevent the formation of alloys. Thus, the development of other kinds of MOF precursors are necessary

as the remaining Zn species might hinder the exploring of reaction mechanism. In addition, it is still a long way to go in optimizing SACs including the metal loading and dispersion of metal sites as well as yields of MOF-derived SACs. Exploring some low-cost MOFs with high-content of carbon and nitrogen or other functional heteroatoms would be greatly helpful for the development of SACs. In this aspect, the combination of MOFs with other functional materials as precursors seems to be efficient.

3. Characterization Methodologies for SACs

Investigating the composition and coordinating structure of SACs is critical for understanding the real active sites during electrochemical processes. To date, there are many characterization tools can be used to identify the structure of SACs. The mostly used techniques are electron microscopy and electron-energy-loss spectroscopy (EELS), X-ray absorption spectroscopy (XAS), and infrared (IR) spectroscopy. Generally, electron microscopy techniques include the aberration-corrected HAADF-STEM and scanning tunneling microscopy (STM), and the X-ray absorption spectroscopy techniques involve the X-ray photoelectron spectroscopic (XPS), EXAFS, and XANES. Because the SACs are isolated metal atoms dispersed on various supports, it is a big challenge to directly observe their structures at atomic levels via just one technique. In most cases, the combination of more than one kind of characterization techniques is necessary. Additionally, the density functional theory (DFT) calculation is a promising tool to predict and verify the structure of SACs as well as the mechanism in a reaction. In this part, we will concisely introduce the application of above-mentioned techniques on revealing spatial structure and coordination environment of SACs.

3.1. Electron Microscopy and EELS Spectrum

Transmission electron microscopy (TEM), having modes of bright-field and dark-field, is an ideal tool to investigate the size and structure of materials. To directly observe the single-metal atoms on supports at the atomic level, an aberration-correction attachment is needed. The HAADF-STEM images with bright spots in subnanometers provide us the basic information to know the position and spatial distribution of metal atoms. The kind of single-, dual-atom catalysts or cluster catalysts can be quickly identified through the direct aberration-corrected HAADF-STEM images. What's more, the surroundings of single-metal atoms as well as their species can be identified with the help of attachments such as microscope EELS. For example, Wu and co-workers reported a Co-SAC by pyrolysis of Co-doped ZIF-8 via an one-step thermal transformation process.[62] The atomic coordination between Co and N species was directly observed by HAADF-STEM images coupled with EELS curves at atom level (**Figure 8**a). Though the HAADF-STEM images and EELS spectra can provide us the direct information of SACs, the test should be operated under high-energy electron beam, which results in the breaking of structures and dynamic migration of metal atoms. To avoid the inaccurate characterizations, experiments are usually operated at a low voltage and low temperature. Thus, the use of low-temperature scanning tunneling microscopy (LT-STM) is more appropriate for analyzing single atoms (Figure 8b).[63]

3.2. IR Spectroscopy

Probe molecule IR spectroscopy is an effective approach to identify and distinguish metal SAs from NPs. Because the adsorbed guest molecules on metal sites will display various vibrational frequencies and intensities, the IR spectroscopy based on monitoring the adsorption behavior of adapted probe molecules can give valuable information about the metal atoms on supports. As the typical probe molecules, CO is widely used due to its sensitive interaction with metal atoms/nanoclusters and small size allowing easy diffusion into samples. For instance, to identify the atomically dispersed Pt atoms in Al–TCPP–0.1Pt, the authors studied the diffuse reflectance infrared Fourier transform (DRIFT) spectroscopy of the samples.[49] After purging with Ar flows to remove loosely adsorbed CO molecules, no band appears in the range 2030–2080 and 1920–1950 cm^{-1} for linear- and bridged-adsorbed CO on Pt nanoclusters or nanoparticles, while a peak located at 2090 cm^{-1} for CO chemisorbed on Pt atoms is observed (Figure 8c). Owing to its high efficiency and sensitivity, IR spectra are widely used for the detection of accessible metal sites in MOFs or MOF-based single-metal sites,[64] which can also monitor the removal process of guest molecules in MOFs or test the stability of MOFs.

3.3. XAS

XAS measurement including XANES and EXAFS spectroscopy is another useful technique to reveal the local geometric, electronic structure and coordination environment of SACs. From the XANES results, the structural information and valence state of adsorbed atoms can be obtained, while the coordination environment of central atoms, such as coordinating numbers, radial distribution, and bond length can be obtained from the EXAFS spectroscopy. In SACs, no metal–metal bond can be observed from EXAFS spectra, but these bonds can be found in dual-atom, cluster, or nanoparticle catalysts. Thus, XAS has become a necessary characterization tool for SACs.

For example, by virtue of XAS, Li and co-workers studied the coordination structure of MOF-derived M–N_x–C catalysts (Figure 8d).[52] From the Fourier transform (FT)-EXAFS curve of Fe-ISAs/CN, only one main peak was observed at around 1.5 Å, which originated from Fe–N(O) scattering paths, and no peak corresponding to Fe—Fe bonds was found at 2.2 Å, suggesting the isolated dispersion of Fe atoms. According to the EXAFS data, the coordination number of Fe was about 5, with an average bond length of 2.01 Å. Fitting results reveal that one Fe atom is coordinated with four N atoms on the carbon plane, and one O_2 molecule is considered to be adsorbed on Fe atom, which is perpendicular to Fe–N_4 porphyrin plane. Taking Fe–Co dual-atom catalyst as another example (Figure 8e), the (Fe,Co)/carbon nanotube (CNT) showed a different Fe K-edge XANES spectrum from Fe_2O_3 and Fe foil.[65] The FT k^3-weighted

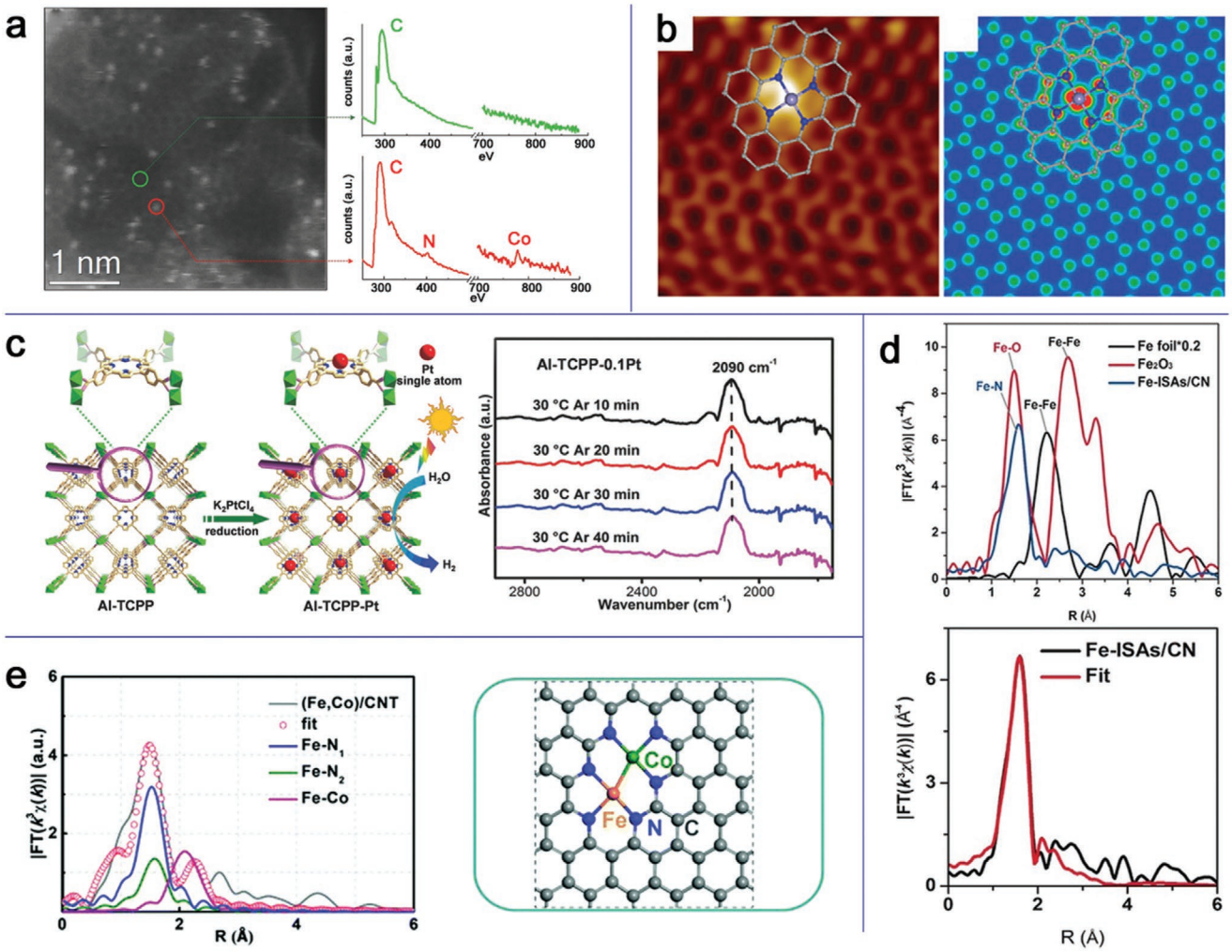

Figure 8. Advanced characterization techniques for SACs. a) Aberration-corrected MAADF-STEM images with the corresponding EEL point spectra. Reproduced with permission.[62] Copyright 2018, Wiley-VCH. b) Low-temperature scanning tunneling microscopy (LS-STM) images of FeN_4 supported on graphene with the simulated STM image. Reproduced with permission.[63] Copyright 2015, American Association for the Advancement of Science. c) Schematic illustration of the synthesis of Al–TCPP–Pt and its DRIFT spectra of CO adsorbed samples after being purged with Ar gas. Reproduced with permission.[49] Copyright 2018, Wiley-VCH. d) Fourier transform (FT) of the Fe K-edge and the corresponding EXAFS *R* space fitting curves of Fe single-atom catalysts. Reproduced with permission.[52] Copyright 2017, Wiley-VCH. e) Fe K-edge EXAFS fitting curves of the (Fe,Co)/CNT with the proposed Fe–Co configuration. Reproduced with permission.[65] Copyright 2018, Royal Society of Chemistry.

X(*k*)-function of EXAFS spectra in *R* space showed a strong peak at about 1.48 Å for Fe—N bonds, which was similar to the FePc with a square planar geometry. It was found that a small peak occurring at about 2.22 Å could be attributed to the formation of metal–metal bonds, which matched well with FeCo nanoparticles supported on carbon nanotubes. Additionally, similar results were obtained from the Co-K-edge XANES spectrum and FT curves. Fitting curves of (Fe,Co)/CNT confirmed that Fe–Co sites were coordinated with three N atoms at each end, forming a unique $FeCoN_6$ configuration with superior ORR performances.

To have more insights into catalysts, it is important to develop the advanced characterization techniques such as in situ or ex situ characterizations. At present, combinating more kinds of techniques to predict or reveal the structure of SACs might be a good choice. As an efficient technique tool, theoretical computations based on DFT are sometimes necessary, which can help us to find the most stable configuration of metal atoms immobilized on supports and determine the possible reaction mechanisms of catalysis process. By combination with DFT calculations, the detail information about catalysts including the formation Gibbs free energy (ΔG), defects, electronic structure, and charge distributions can also be obtained, allowing us to understand the catalysts at the atomic level.

4. Electrocatalytic Applications

SACs with isolated metal sites have attracted extensive attention in the field of catalysis because of their remarkable catalytic performances and maximum of atom utilization. As a new frontier in electrocatalytic fields, SACs provide a feasible solution

for solving the excessive consumption of noble metals. Even at a very low loading of metals, the catalysts exhibit boosting catalytic activities and attractive TOF values by fully using metal atoms located on supports. In addition, carbon-supported SACs synthesized by pyrolysis of MOFs often own the features of large surfaces areas, high pore volume, rich-exposed active sites, and good conductivities and stabilities, endowing them a promising future for energy storage and conversion. To date, MOF-derived SACs have been widely studied in ORR, OER, HER, CO_2RR, NRR, and others. In the following part, we will discuss their applications on these fields separately.

4.1. Oxygen Reduction Reaction

As a basic reaction in fuel cells, ORR has been widely studied. The reduction of O_2 in electrolytes has two pathways: two-electron pathway for peroxide (H_2O_2) and four-electron pathway for water (H_2O), both of which can be detected in productions, and the percentage of each is highly depended on the activities of catalysts. Among various catalysts, Pt-based catalysts are considered as the best ORR catalysts as far as we know.[66] However, the wide spread of Pt-based catalysts is limited by the scarcity and high cost in practical applications. To decrease the costing of noble metals, the synthesis of Pt-SACs is a good choice, which keeps the high-efficiency Pt sites and largely decreases the cost of catalysts.[67] The catalytic activity of Pt-related catalysts can be improved by increasing the loading of Pt or changing the structure of support materials, such as heteroatoms doping or using 3D interconnected structures. These important works can be acquired from previous reports.[68] In the following section, we will focus on the development and applications of non-noble metal SACs derived from MOFs.

In noble-metal-free catalysts, the typical catalysts about Fe–N–C are extensively studied.[54,69] It is demonstrated that electrocatalytic performances of transition metals in M–N_x–C follow the order of Fe > Co > Mn > Cu > Ni. Sometimes, the Fe–N_x–C species even display a superior property to noble-metal catalysts. To date, MOF-derived Fe-SACs have been widely investigated in ORR. Jiang et al. developed a series of Fe–N–C nanocatalysts with controllable density of Fe–N_4 sites (**Figure 9**a–d).[69a] The hierarchical micro–mesoporous carbon with proper amounts of Fe doping, named as Fe SAs–N/C-20, exhibited a superior ORR activity, which showed a half-wave potential of 0.915 V in alkaline conditions and good stability (Figure 9e,f). Theoretical calculation results suggested that edge-hosted Fe–N_4 sites obtained by porosity engineering could reduce the ORR barriers compared to intact atomic configuration. Generally, the introduction of pores in catalysts by engineering strategies is a good approach to enhance their performances. In our group, we developed an overhang-eave like carbon cage with isolated Fe single atoms (Fe/OES) to boost the utilization of metal sites. The resulted catalysts exhibited a high TOF value of 25 s^{-1}, which was about five times of the single Fe immobilized on bulk carbon (5.4 s^{-1}).[7a] Hierarchical pores with interconnected 3D structures would extensively expose the interior active sites and enhance the accessible metal sites, which can also accelerate the products and electrolytes transfer during catalysis process, resulting in the superior electrocatalytic properties.[17] For example, the hierarchical porous Fe_{SA}–N–C with large surface areas for Fe active sites immobilization and mass transportation displayed a larger kinetic current density of 23.27 mA cm^{-2} at 0.85 V, which was about four times higher than that of Pt/C catalysts (5.61 mA cm^{-2}).[54] Controlling the coordination environment of Fe metal centers is another approach for enhancing the catalytic activities of SACs. Different kinds of Fe–N_x with coordination numbers of two to five have been synthesized and studied by Lai et al.[69b] The five-coordinated N–Fe–N_4 structure exhibited a good ORR performance in 0.5 M H_2SO_4 aqueous, showing a comparable activity than 30% Pt/C catalysts. The boosting activity of N–Fe–N_4 is attributed to the reducing energy barrier and decreasing adsorption energy of OH groups on metal sites.

To improve the catalytic performances of SACs, heteroatoms doping in supports are quite efficiency. Apart from the mostly studied N atoms, the S or P doping within the skeleton of carbon matrix is feasible for changing the coordination environment and tuning the electronic structure of metal centers. Li and co-workers prepared the N, S, P tridoped hollow carbons with highly distributed single Fe active sites (Figure 9g,h).[32c] Benefiting from the unique hollow morphology of carbon cages and electronic structure of metal centers that accelerate ORR kinetics, the obtained Fe-SAs/NPS-HC displayed a superior ORR performance to Pt/C catalysts, showing a half-wave potential of 0.912 V in 0.1 M KOH and 0.791 V in 0.5 M H_2SO_4 aqueous solutions (Figure 9i). A large kinetic current density of 71.9 mA cm^{-2} was obtained for Fe-SAs/NPS-HC at the potential of −0.85 V, which was 15 times higher than that of Pt/C. The Fe-SAs/NPS-HC also showed a small Tafel slope of 36 mV dec^{-1} (Figure 9j), demonstrating the outstanding catalytic activity of this catalyst toward ORR. Owing to its excellent ORR performances, the Fe-SAs/NPS-HC was used as the cathodes for Zn–air battery and H_2–air fuel cell. The constructed Zn–air battery showed an open-circuit voltage of 1.45 V with a maximum power density as high as 195.0 mW cm^{-2} and high current density of 375 mA cm^{-2} (Figure 9k). In addition, the Fe-SAs/NPS-HC-based membrane electrode device also showed a good performance at the testing temperature of 60 °C, giving a maximum power density of 333.0 mW cm^{-2} at 0.41 V (Figure 9l), which reached to 400 mW cm^{-2} under 80 °C. The results suggested that the codoping of P and S in N-doped carbons with unique hollow features can enhance ORR kinetics by the structure functionalities and electronic control of metal atoms. To have more insights into the relationships between structure and performance, Shui and co-workers fabricated a concave-shaped Fe–N–C SACs with large mesopore volumes and external surface areas, and its performance in proton exchange membrane fuel cells (PEMFCs) was studied.[70] The concave-shaped Fe–N–C SACs were prepared by the modulation of SiO_2 on the surface of ZIF-8, leading to the formation of concave carbons with increased surface areas and mesopore volumes. It was proved that the mesopore and external surface area was vital for both enhancing the mass transport between catalyst layers and maximizing the exposure of Fe–N_4–C_8 moieties, which were the predominant factors in determining the catalytic activity of Fe–N–C in fuel cells. The synthesized catalysts exhibited high activity with a four-electron pathway, superior stability, and outstanding methanol tolerance in rotating disk electrode (RDE)

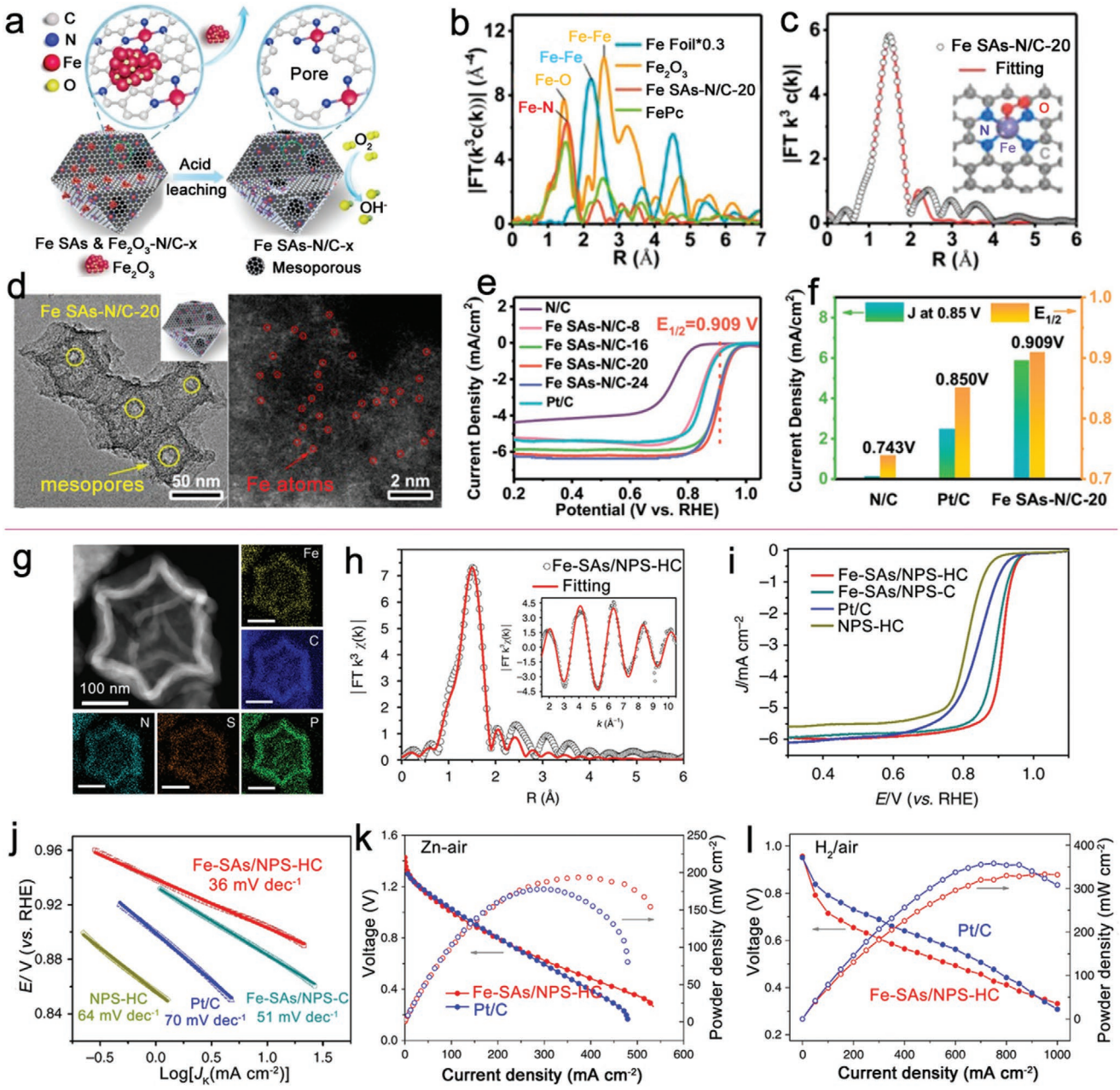

Figure 9. a) Schematic illustration for the synthesis of edge-hosted Fe–N_4 moieties; b) FT k^3-weighted EXAFS spectra; c) the fitting curves of Fe SAs–N/C-20; d) HRTEM and HAADF-STEM image of Fe SAs–N/C-20; e) LSV curves of Fe SAs–N/C-*x*; f) the comparison of current density and half-wave potentials. Reproduced with permission.[69a] Copyright 2018, American Chemical Society. g) HAADF-STEM image and element maps of Fe-SAs/NPS-HC; h) EXAFS fitting curves; i) ORR polarization curves of prepared Fe single-atom catalysts and control samples; j) Tafel plots; k) discharging polarization curves and power density plots for Zn–air batteries; l) H_2–air fuel cell polarization curves and power density plots of Fe-SAs/NPS-HC. Reproduced with permission.[32c] Copyright 2018, Nature Publishing Group.

measurements. The constructed PEMFCs by using this catalyst showed a high kinetic activity at 2.5 bar H_2–O_2, with a peak power density of 1.18 W cm^{-2} at 0.47 V. Even at 1.0 bar H_2–O_2, a high current density of 129 mA cm^{-2} at 0.8 V (iR-free) was obtained, evidencing the great potentials of Fe-based SACs for PEMFCs applications.

Although Fe–N–C catalysts showed the best ORR catalytic activity with relatively high half-wave potential about 0.8 V (vs RHE), the Fe-based catalysts are not the best choice for PEMFCs because the formed Fe^{2+} or Fe^{3+} ions during the catalytic process will react with H_2O_2 leading to the formation of hydroxyl and hydroperoxyl radical species. The obtained free radicals can attack the PEMFC ionomer and membrane, resulting in the degradation of performance and even cell failure.[71] As a member in transition metals, Co-based SACs have also been widely studied for ORR. Using the bimetallic

ZnCo-ZIF as precursors, Co-SACs with a loading of Co species as high as 4 wt% were prepared, showing a much higher half-wave potential of 0.881 V than commercial Pt/C (0.811 V).[14] By controlling the carbonization temperatures, the Co–N_x with different coordination numbers could be achieved. Under 800 °C, the produced metal sites were Co–N_4, while this coordination structure changed into Co–N_2 moieties at 900 °C. The Co–N_2 sites with a stronger interaction for H_2O_2 showed a better catalytic activity than Co–N_4 species, displaying a four-electron pathway for ORR. This inspires us to design SACs with proper coordination structures to improve their properties in different reaction conditions. It was reported that the Co–N_4 species exhibited an excellent ORR performance in acid media. The prepared Co–N–C catalysts from the carbonization of Co-doped ZIF-8 showed a half-wave potential of 0.8 V versus RHE and superior stability in 0.5 M H_2SO_4, comparable to the Fe–N–C and Pt/C catalysts in acid electrolytes.[62] The high-performance of Co–N–C catalysts in acid media is attributed to the high density and uniformly distributed Co–N_4 species, which have been successfully embedded into 3D porous carbons under high calcination temperatures and result in an excellent stability in acid electrolytes. This catalyst was used as the cathode for H_2/O_2 fuel cells and displayed a good performance with the highest power density of 0.56 W cm^{-2}. A power density of 0.28 W cm^{-2} could be achieved even in H_2–air batteries. The desirable Co-SACs with good activity and excellent stability hold a great promise to solve the Fenton reagent problems associated with Fe-based catalysts in PEMFC. Generally, modulating the composition and structure of MOF precursors, the performance of Co-SACs can be adjusted easily. A core–shell structured Co–N–C nanocatalyst was designed by a surface-assisted MOF approach.[60] The results showed that the synthesis process is beneficial for the formation of Co–N_{2+2} sites, a Co–N_4 moiety that bridge over two adjacent armchair graphitic edge (**Figure 10**a). Compared to the Co–N_4 species embedded fully in the intact graphitic layer, the Co–N_{2+2} sites on the edge of carbon layers are more active for ORR (Figure 10b). The resulting catalysts (Co–N–C@F127) gave a half-wave potential as high as 0.84 V (vs RHE) in acid electrolyte along with a dominant four-electron pathway (Figure 10c,d). Attributed to the high activity and excellent stability in acid condition, Co–N–C@F127 catalysts exhibited a large half-wave potential after 30 000 cycles of CV testing, only 40 mV lower than the first cycle (Figure 10f).

Cu-SACs with Cu–N_4 coordinating configuration are proved to be a good ORR catalyst in alkaline conditions. Recently, Qu et al. developed a NH_3-assisted gas-transport approach to deposit isolated Cu atoms on a ZIF-8-derived porous carbon.[26] Under the NH_3 flow at high temperature, the bulk Cu foam will change to Cu(NH_3)$_x$ species, which can be trapped by N sites on porous carbon yielding a Cu-SAs/N–C catalyst. The resulting catalysts showed a large surface area of 832 m^2 g^{-1} with high densities of exposed Cu–N_4 active sites (about 0.5 wt% Cu). Thus, Cu-SAs/N–C catalysts exhibited an excellent ORR activity with a half-wave potential of 0.895 V, much positive than the Pt/C and Cu_{NP}/N–C catalysts. RRDE measurements indicated a four-electron pathway over Cu-SAs/N–C. A small Tafel slop of 63 mV dec^{-1} is obtained, confirming its good kinetics. Even tested for 5000 cycles, the Cu-SAs/N–C catalysts displayed a negligible loss in activity with the unchanged Cu–N_4 coordination structures. This work also provided a feasible strategy for preparing SACs in a large scale.

To promote the practical use of SACs in PEMFCs, catalytic performances in acid media are important. Investigations showed that Mn-based catalysts might have the potential applications in PEMFCs, owing to their weak reactivity for H_2O_2 compared to the Fe or Co catalysts. Wu and co-workers developed a Mn-SAC with Mn–N_4 coordination structure by a two-step doping and adsorption process (Figure 10f–h).[35] The pyrolysis of Mn-doped ZIF-8 can result in a porous carbon with Mn single atoms immobilization. To increase the density of Mn-active sites, the obtained porous carbon in the first step is used as a host for adsorbing additional Mn and N sources. After a secondary thermal activation, the resulting Mn-SACs exhibited a promising ORR activity and stability in acid electrolytes. The synthesized Mn–N–C catalysts, with a Mn content of 3.03 wt%, showed a half-wave potential of 0.8 V (vs RHE) with a four-electron pathway, only 60 mV lower than Pt/C catalysts and comparable to the Fe- and Co-related catalysts obtained from the same method (Figure 10i). DFT calculations suggested that the Mn–N–C catalyst with a Mn–N_4–C_{12} structure showed favorable binding energy with O_2, OOH and H_2O, which could overcome the energy barrier for breaking O—O bonds and completing the $4e^-$ reduction. After 30 000 cycles, only a loss of 17 mV in half-wave potential is observed for this Mn–N–C catalyst. In addition, the catalyst could keep 88% of the initial current density after tested for 100 h at 0.7 V, indicating its excellent activity and stability in acid conditions. When used as the cathode in membrane electrode for H_2–O_2 fuel cells, the high open-circuit voltage of 0.95 V and power density of 0.46 W cm^{-2} were obtained (Figure 10j). At a partial pressure of 1.0 bar, the constructed cell exhibited the current density of 0.35 and 2.0 A cm^{-2} at 0.6 and 2.0 V, respectively.

Compared to the above mentioned Fe, Co, Mn, and Cu, Zn has a fully filled d orbital that cannot convert to high-valence oxidative ion. Thus, Zn-related catalysts usually show a poor ORR performance. Although a few studies revealed that Zn–N_4 structures also exhibited promising ORR activities in both acid and alkaline solutions, the activity of Zn-SACs is still far from than Fe–N–C catalysts. However, Zn is difficult to be oxidized into high valence state, which is less harmful to electrode and electrolyte membrane, and Zn–N_4 sites are more stable than Fe–N_4 sites in acid media. Therefore, Zn-SAC is also a kind of potential candidates for fuel cells.[72]

To further enhance the ORR performance of SACs, adjusting the active species of catalysts is useful, and the combination of two or more kinds of metal sites in catalysts can improve the catalytic performances through synergistic effects between these metal species.[17,65,73] The mixed-metal SACs can be easily prepared by using MOF composites as precursors. Up to date, the most widely studied multimetal SACs are FeCo-SACs, which exhibit a superb ORR performance in both acid and alkaline conditions. Fe–Co dual atoms located on a hollow carbon framework with porphyrin-like Fe–Co dual sites were obtained from the pyrolysis of ZIF-8 encapsulated with Fe and Co guest ions in cavities.[73d] The obtained catalysts with Fe–Co dual sites afforded an outstanding ORR activity, superb stability, and high methanol/CO tolerance under acidic electrolyte. Benefiting from the Fe–Co dual sites that are favorable for dissociating

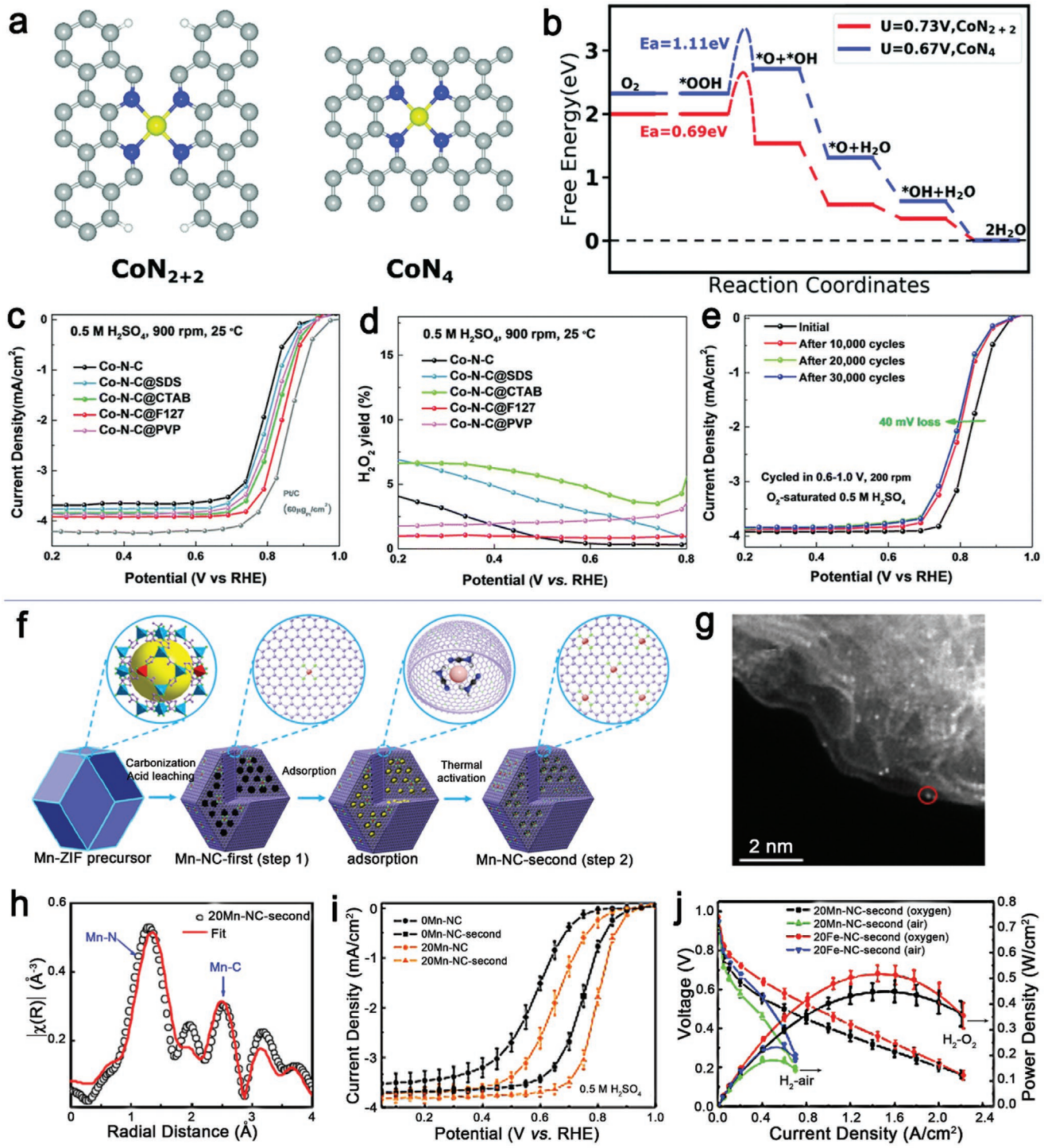

Figure 10. a) Atomistic structure of CoN_{2+2} and Co–N_4 active sites on N-doped carbon supports; b) calculated free energy evolution diagram for four-electron pathway on CoN_{2+2} and Co–N_4 sites; c) ORR polarization plots and d) H_2O_2 yields for the catalysts in 0.5 M H_2SO_4 electrolyte; e) potential cycling stability test of Co–N–C@F127 catalysts. Reproduced with permission.[60] Copyright 2019, Royal Society of Chemistry. f) Schematic for the synthesis of atomically dispersed MnN_4 catalysts. g) Aberration-corrected MAADF-STEM image; h) the fitting results of Mn K-edge EXAFS data; i) ORR polarization plots in 0.5 M H_2SO_4 electrolytes; j) fuel cell performances of the best-performing catalysts in H_2/O_2 and H_2/air conditions. Reproduced with permission.[35] Copyright 2018, Nature Publishing Group.

O–O bands and reducing the energy barrier to break O–O band, the as-prepared FeCo-dual catalysts showed a half-wave potential of 0.863 V and onset potential of 1.03 V, comparable to the best ORR catalysts tested in alkaline conditions (**Table 1**). When used as the catalysts for H_2–air fuel cell, the cell displayed a peak power density of 505 mW cm^{-2} at 0.42 V and a

Table 1. Summary of SACs derived from MOF precursors for oxygen reduction reaction.

Catalyst	MOF precursor	Metal configuration	Metal content	Electrolyte	Performance			Refs.
					$E_{1/2}$[a)] [V]	N[a)]	Stability	
Fe/OES	Fe/ZIF-8@SiO_x	Fe–N_4	0.11 wt%	0.1 M KOH	0.85	3.8–4.0	Slight decrease after 3000 CV cycles	[7a]
Fe–N/GNs	s-Fe/ZIF-8/GO	Fe–N_x	2.04 wt%	0.1 M KOH; 0.1 M $HClO_4$	0.903 0.837	3.98	19 mV negative shift in alkaline solution; no obvious shift in acidic medium	[24]
FeSAs/CNF-900	$Zn_{10}Fe_1$-ZIF	Fe–N_x	4.58 wt%	0.1 M KOH	0.89	3.93–3.98	No significant loss in $E_{1/2}$ and diffusion-limited current after 5000 cycles	[47a]
Co–N–C@F127	Co-ZIF-8@F127	CoN_{2+2}	1.0 at%	0.5 M H_2SO_4	0.84	≈4	40 mV loss after 30 000 CV cycles	[60]
TPI@Z8(SiO_2)-650C	TPI@Z8 (SiO_2)-650	Fe–N_4–C_8	2.78 wt%	0.5 M H_2SO_4	About 0.8	>3.6	No decrease in current density via chronoamperometry test at 0.5 V for 10 000 s	[70]
CoFe@C	CoFe@MET-6	Co–N_4; Fe–N_4	Co: 0.5 wt%; Fe: 0.37 wt%	0.1 M KOH	0.89	3.9	Keep 88% of initial current density after 20 000 s	[17]
Co–N–C-10	$Zn_{10}Co_1$-ZIF	Co_2–N_5	4.3 wt%	0.1 M $HClO_4$	0.79	≈4	12 mV loss after 20 000 CV cycles	[47d]
20Co-NC-1100	CoZn-ZIF	Co–N_4	0.3 at%	0.5 M H_2SO_4	0.8	≈4	30 mV loss after 10 000 CV cycles	[62]
Cu-SAs/N–C	Cu foam and ZIF-8	Cu–N_4	0.54 wt%	0.1 M KOH	0.895	3.96	No loss after 5000 CV cycles	[26]
Fe–N–C-950	Fe-ZIF-8	Fe–N_4	0.32 wt%	0.1 M $HClO_4$	0.78	4	12 mV negative shift in $E_{1/2}$ after 10 000 cycles	[56]
Fe SAs–N/C-20	FePc@ZIF-8	Fe–N_4	0.20 wt%	0.1 M KOH	0.915	3.8	Negligible loss after 10 000 CV cycles	[69a]
FeSA–N–C	Fe20-PCN-222	Fe–N_4	1.76 wt%	0.1 M KOH; 0.1 M $HClO_4$	0.891 0.776	4 4	Eligible decay of activity after 5000 CV cycles in base; 6 mV decay after 5000 cycles in acid	[54]
Fe-SAs/NPS-HC	ZIF-8/Fe@PZS	Fe–N_4	1.54 wt%	0.1 M KOH; 0.5 M H_2SO_4	0.912 0.791	3.96–3.99 3.95	No obvious decay after 5000 CV cycles in KOH; 5 mV loss after 5000 CV cycles in acid solution	[32c]
20Mn-NC-second	Mn-ZIF-8	Mn–N_4	3.03 wt%	0.5 M H_2SO_4	0.8	≈4	17 mV loss after 30 000 CV cycles	[35]
(Fe,Co)/N–C	Fe,Co-doped ZIF-8	(Fe,Co)–N_6	Fe: 0.93 wt%; Co: 1.17 wt%	0.1 M $HClO_4$	0.863	4	No decrease in $E_{1/2}$ after 5000 CV cycles	[73d]
Fe/N-GPC	FeD@MIL-101-NH_2	Fe–N_4	1.1 wt%	0.1 M KOH	–	≈4	Remaining more than 95% of current density after 20 000 s	[48]
Fe-ISAs/CN	Fe(acac)$_3$ @ZIF-8	O_2–Fe–N_4	2.16 wt%	0.1 M KOH	0.9	3.9	Nearly no change after 5000 CV cycles	[52]
Co SAs/NC (900)	Zn/Co-MOF	Co–N_2	4.3 wt%	0.1 M KOH	0.881	≈4	No loss after 5000 CV cycles	[14]

[a)] $E_{1/2}$ stands for the half-wave potential; N stands for the electron number.

large current density of 550 mA cm^{-2} at 0.6 V. As supports are of vital importance for the catalytic activity of SACs, immobilization of single-metal atoms on a proper support can boost its catalytic activity. In this side, the Fe–Co dual sites decorated on N-doped carbon nanotubes exhibited the ultrahigh half-wave and onset potentials of 0.954 and 1.15 V, respectively, which were much higher than those of Pt/C and superior than most reported noble-metal-free catalysts.[65] The Zn–air battery constructed by this Fe–Co/dual-atom catalyst showed high voltages of 1.31 and 1.23 V at the discharge current density of 20 and 50 mA cm^{-2}, respectively. In another work, the Fe and Co single atoms decorated on MOF-derived carbons exhibited good ORR performances in alkaline conditions with the half-wave potential of 0.972 V.[73a] Using Fe/Co-doped Zn-based triazole-rich energetic MOFs as a precursor, submillimeter-scaled FeCo@C catalysts with hierarchical pores have been prepared by Xu and co-workers. The individual Fe- and Co-immobilized catalysts showed excellent ORR activity in both acid and alkaline conditions, with an unexpected high half-wave potential of 0.886 V in 0.1 M KOH.[17] Adjusting the species of metals in dual sites, the ORR performance of dual-atom catalysts can be further enhanced. The Pt–Co dual site catalysts (denoted as A-CoPt-NC) with a Co content of 1.72 wt% and a very small amount of Pt (0.16 wt%) could achieve a half-wave potential as high as 0.96 V in alkaline condition, which is 90 mV positive than that of Pt/C.[74] The ORR mass activity of A-CoPt-NC is 267 times higher than Pt/C in alkaline electrolyte, which might be attributed to the synergetic effect between Pt and Co, leading to the

charge redistribution and d orbital shift in (Co–Pt)@N8V4 coordination.

4.2. Oxygen Evolution Reaction

As a half reaction taking place at the anode, the OER is very important for water splitting. In the past decades, various kinds of catalysts with or without carbon species have been studied for OER, which exhibit promising performances in alkaline conditions. However, the activities and stabilities of these catalysts in acid conditions need a further improvement. Increasing the utilization of metal sites is an efficient approach for enhancing OER performances.[75] Through a salt-template method, monodispersed Co atoms on a N-doped carbon support with a metal content as high as 15.3 wt% have been achieved by the pyrolysis of ZIF-67@KCl composites.[76] The resulting catalysts showed excellent bifunctional catalytic activities for ORR and OER. In ORR testing, the half-wave potential of 0.91 V and Tafel slope of 70 mV dec^{-1} were obtained, much better than those of Pt/C catalysts. When carried out in OER measurements, the Co-SACs displayed a relatively low potential of 1.54 V reaching the current density of 10 mA cm^{-2} with a very low Tafel slope of 74 mV dec^{-1}. In addition, the catalysts owned superb stability, with 86% of the current density retention after 200 000 s at 1.54 V. Owing to the bifunctional performances of this catalyst, it showed a very low overpotential of 0.63 V ($\Delta E = E_{j=10} - E_{1/2}$) for the high-performance Zn–air battery. The constructed Zn–air battery showed an open-circuit voltage of 1.49 V, a good specific capacity, and a large energy density. It was demonstrated that the Co–N_4 active sites decorated on graphene-like carbons were responsible for the high performance.

Generally, the OER catalytic activities can be improved by adjusting the supports and metal species. Using the graphene as supports, the OER activity of single transition metals immobilized on N-doped graphene follows the trend of Ni > Co > Fe in alkaline conditions.[77] However, due to the corrosion of catalysts during the OER process, most SACs showed a poor stability and unsatisfied activity. Engineering coordination environments of immobilized metal centers is vital for modifying their electronic and geometric properties, which might greatly affect the electrocatalytic activity and stability of SACs. Very recently, we developed a kind of dual-atom iron catalysts (Fe-DACs) via a heteroatom modulator approach, and the resulting Fe-DACs exhibited excellent OER and Zn–air battery performances.[15a] As shown in **Figure 11**a, the individually dispersed Fe dual-atoms are obtained by adjusting the composition of encapsulated metal clusters in MOF channels with a following carbonization process. When using trinuclear $Fe^{III}{}_2Fe^{II}$ complex as the guests, Fe nanoclusters immobilized on graphitized N-doped carbon layers (GNCL) are synthesized owing to the aggregation of Fe atoms through the Ostwald-ripening process. The stable Fe dimer coordinated with N defects on carbon layers are obtained by replacing $Fe^{III}{}_2Fe^{II}$ with $Fe^{III}{}_2Co^{II}$ and $Fe^{III}{}_2Zn^{II}$ in MOF precursors. Well-defined Fe dual-atoms on carbon layers are identified by direct TEM imaging (Figure 11b) and X-ray absorption fine structure (XAFS) analyses (Figure 11c,d). The theoretical calculation indicates that the formation of dual iron atoms with Fe_2–N_6 configurations need a formation energy of −3.25 eV (Figure 11e), which is less than those for Fe_3–N_4 (−2.58 eV) and even single atom of Fe/Co–N_4 (−1.99/−2.14 eV). Benefiting from its unique Fe–Fe sites coordinated with N species on carbon supports, the Fe-DACs exhibited excellent OER performances with an overpotential of about 350 mV at 10 mA cm^{-2}, much lower than those of Fe nanoclusters, Fe/Co single-atom catalysts, and commercial IrO_2 catalysts. Besides the superb activities, the Fe dual-atom structure can also promote the OER kinetics, showing a small Tafel slope as low as 66 mV dec^{-1}. Such a small Tafel slope can be attributed to the decrease of energy barrier on this unique Fe_2–N_6 sites. When using as the cathode for Zn–air batteries, Fe_2/Co_1-GNCL assembled zinc–air battery can work stably with a superior peak power density of 218 mW cm^{-2}, larger than that of state-of-the-art Pt/C-IrO_2 catalysts (101 mW cm^{-2}). The outstanding performance is possibly ascribed to robust atomically dispersed Fe–Fe sites with the ultrahigh catalytic activity.

It should be noted that the transition metal-based single- or dual-atom catalysts are usually used in an alkaline condition, which is not stable in acid electrolytes owing to the easy dissolution of metal species and carbon supports under the serious OER electrocatalytic environment. To solve this problem, the development of noncarbon SACs, such as metal- or oxide-supports,[78] seems to be efficient. However, MOF-derived noncarbon SACs is just a view in mind, which has not been achieved in laboratory.

4.3. Hydrogen Evolution Reaction

The HER is a fundamental reaction in electrocatalysis and takes place at the cathode during water splitting. In acidic solutions, the H_2 are obtained through the route of $2H^+ + 2e^- \rightarrow H_2$; while in the base solution, H_2 are generated via the process of $2H_2O + 2e^- \rightarrow H_2 + 2OH^-$. At present, insights into mechanisms on acid HER are more thorough than alkaline HER including the hydrogen adsorption behavior and water dissociation process. In HER process, the generation of H_2 from water usually undergoes a multistep reaction, which may proceed via the Volmer–Heyrovsky or Volmer–Tafel mechanism.[79] As far as we know, the Pt-based catalysts are the most efficient catalysts for HER owing to the nearly zero hydrogen adsorption free energy of Pt, while they suffer from the scarcity and high costs.[80] Benefiting from the maximum utilization of metal sites, Pt single-atom catalysts show great potential in HER applications. Isolated Pt atoms located on N-doped porous carbon matrix exhibited a much higher mass activity (up to 25 times) than 20 wt% Pt/C.[80b] However, in practical applications, the large-scale productions are still limited by the scarcity despite the great progress on Pt-based SACs has been achieved. Therefore, the development of non-noble metal SACs is urgently desired.[81] For example, Ni-SACs could achieve the high activity and durability for HER in 0.5 M H_2SO_4 aqueous solution,[50] and some of them even showed bifunctional catalytic performances for HER and OER.[82] Taking the advantage of MOF-strategy, tungsten (W) atoms decorated on N-containing porous carbons (W-SAC) with a coordination structure of $W_1N_1C_3$ have been prepared, which showed an outstanding HER activity. In alkaline electrolyte, it displayed a very low overpotential of 85 mV

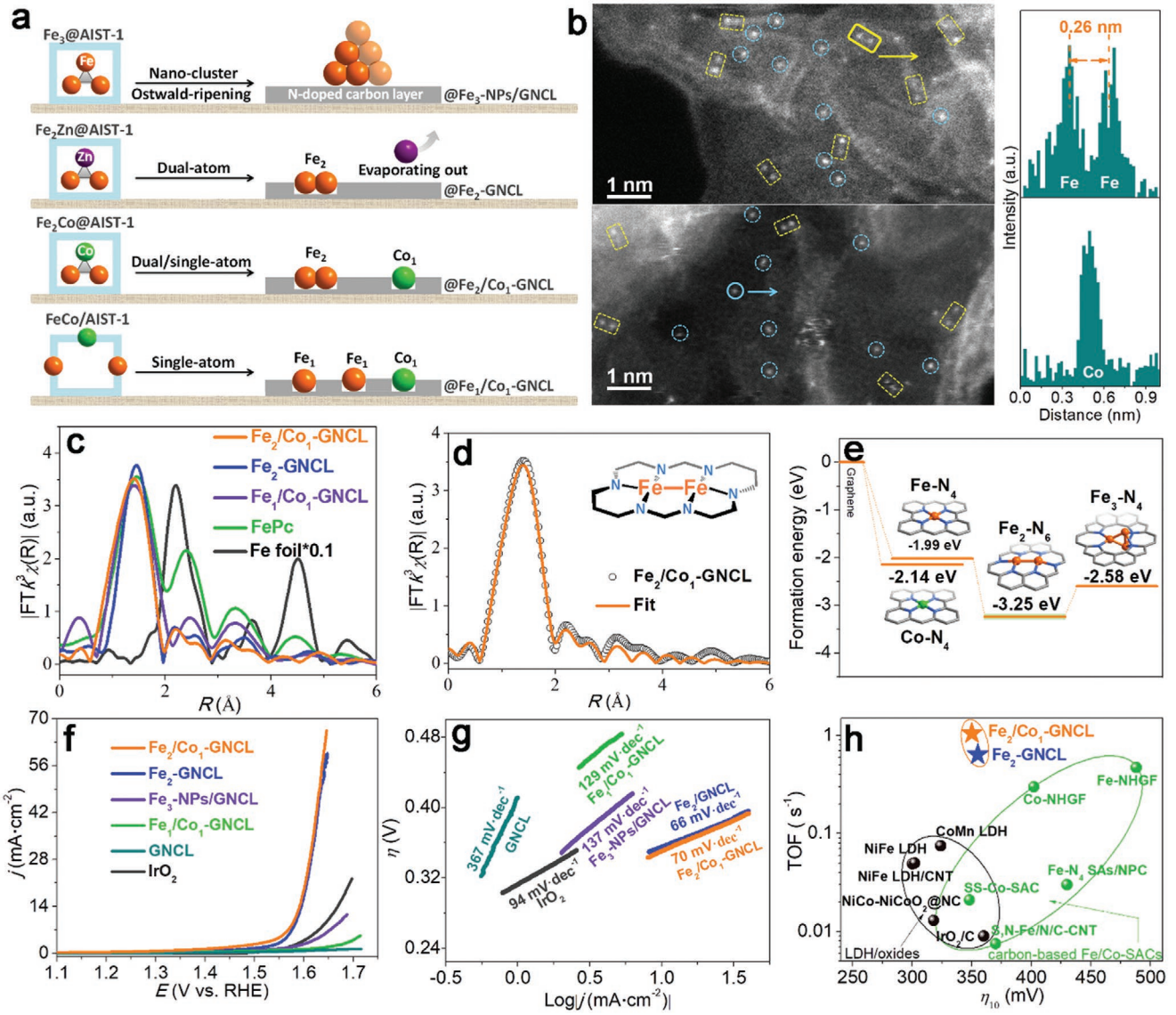

Figure 11. a) Synthesis of dual-atom Fe catalysts by the heteroatom modulator process. b) HAADF-STEM images of Fe_2/Co_1-GNCL, the right pictures showing the intensity profiles of the atomic pair; c) FT k^3-weighted EXAFS spectra; d) the Fe K-edge EXAFS fitting curves; e) formation energies of different kinds of Fe-related moieties on graphene supports; f) OER polarization curves in 1 M KOH electrolyte; g) the corresponding Tafel slope curves; h) the comparing TOF values of Fe_2/Co_1-GNCL with other reported OER catalysts. Reproduced with permission.[15a] Copyright 2020, Wiley-VCH.

reaching 10 mA cm^{-2} and a Tafel slope as low as 53 mV dec^{-1}; and even in 0.5 M H_2SO_4 solution, the W-SAC showed an overpotential of 105 mV with the Tafel slope of 58 mV dec^{-1}. Usually, a smaller Tafel slope is beneficial to HER process, which highly depends on the conductivity and activity of the catalysts. Such a small Tafel slope of W-SAC indicates the fast kinetic process with a good mass-transfer capacity over the catalysts. No appreciable performance degradation is observed after 10 000 CV cycles, suggesting the superb stability of this kind of catalysts. The high activity and long durability of W-SAC are attributed to the unique coordinating structure of $W_1N_1C_3$, which results in a strong interaction between individual W atoms and N-doped carbon supports. After immobilized with W single atoms, the electron structures of coordinated carbon atoms are different. The density of states of W-SAC near the Fermi level, which is mainly contributed by the W d-orbital, is higher than WC and WN, showing a larger carrier density for enhancing charge transfer and thus improving the HER catalytic activity.[55]

Since the coordination environments are significant for the catalytic performance of SACs, changing the coordinated atoms between metal and carbon supports might be a promising strategy for improving the electrochemical property of single-atom catalysts. In carbon-based SACs, the most common structure is $M–N_4$, in which the N can be partially replaced by other atoms, such as phosphate (P). Via the carbonization of triphenylphosphine (PPh_3) encapsulated within a Co-MOF, the catalysts with one Co single atom coordinated with one P atom and three N atoms ($Co_1–P_1N_3$) were prepared (**Figure 12**a).[83]

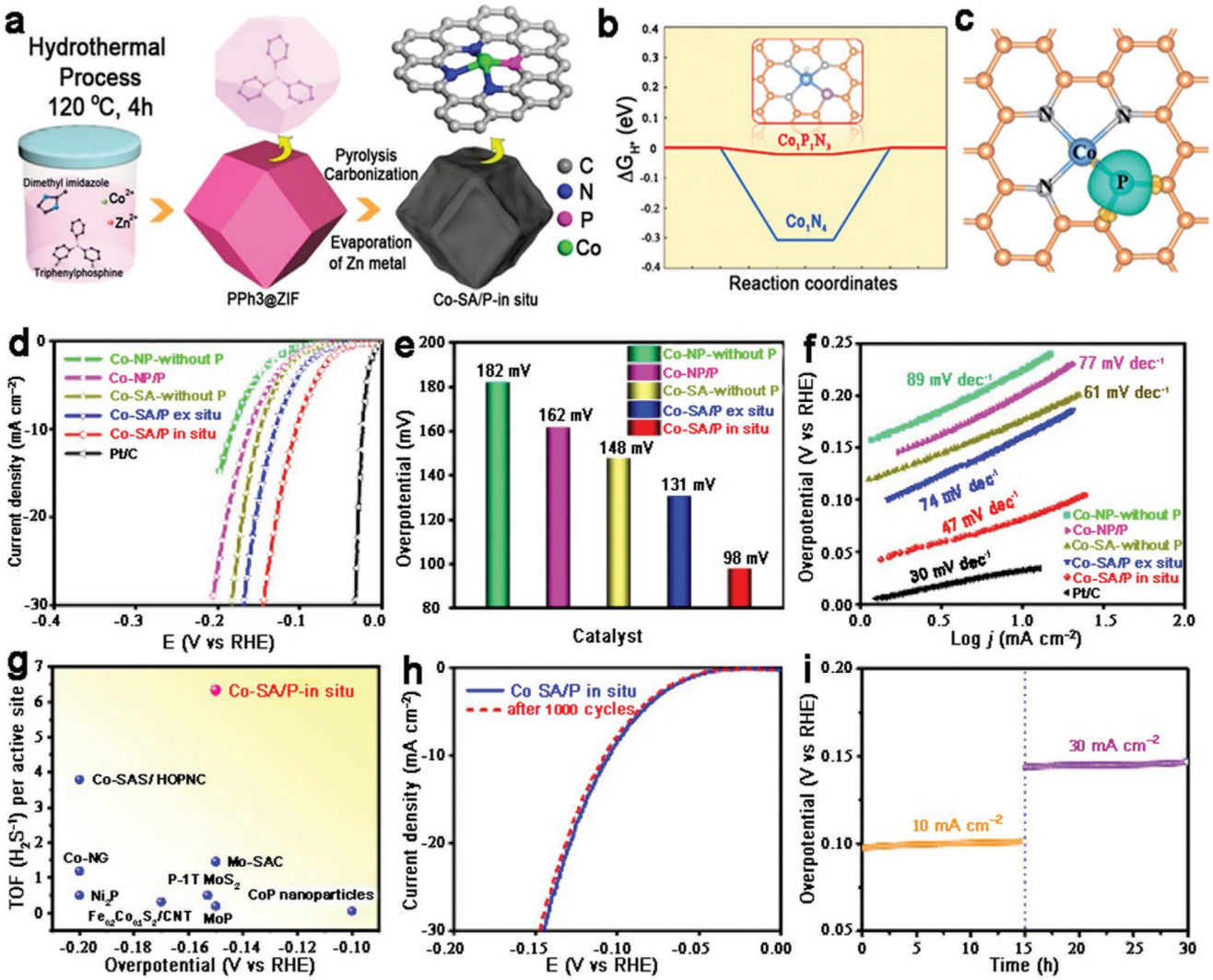

Figure 12. a) Synthesis of Co-SA/P in situ catalysts; b) reaction energy of H adsorption on the surface of Co-SA/P in situ; c) charge transfer of CoP_1N_3 configuration. d–i) Electrocatalytic HER performances of Co-SA/P in situ and other compared catalysts in 0.5 M H_2SO_4 electrolyte. Reproduced with permission.[83] Copyright 2020, American Chemical Society.

The synergistic effects between P, N, and C are essential for the improvement of HER activity. When Co is co-stabilized by P and N, more charge depletion is generated on P, thus resulting in the charge accumulation on surrounding carbon atoms. This unique Co_1–P_1N_3 moiety benefits the electron transfer between Co, P, and N, which has been demonstrated to be essential for electrochemical reactions. DFT calculations demonstrated that the improved catalytic activity is attributed to the optimal reaction Gibbs free energy of hydrogen adsorption (ΔG_{H^*}) on the surface of Co active sites (Figure 12b,c). Compared to the Co_1–N_4 configuration with a ΔG_{H^*} of 0.306 eV, the Co_1–P_1N_3 possessed a much lower ΔG_{H^*} of 0.022 eV, demonstrating its good capability to accelerate the hydrogen adsorption during HER process. Taking the advantage of its unique coordination structure, the as-synthesized Co-SA/P in situ exhibited good HER activities and excellent stabilities (Figure 12d–i), which showed a low overpotential of 98 mV at 10 mA cm^{-2} with a Tafel slope of 47 mV dec^{-1} in the acidic media, much superior to those of Co_1–N_4 structures. Additionally, this synthetic approach is available to design other metal-based (Mn, Fe, Ni, Cu) SACs with similar structures for electrochemical applications.

The electrocatalytic water splitting involving OER and HER is a promising process for renewable energy sources, while the relatively large overpotentials of both reactions are the main barrier for the development of this technique. Usually, the Tafel slope is used to determine the reaction kinetics during HER and OER performances, and a small Tafel slope is highly desirable. Increasing the intrinsic conductivity of the catalysts and exposing more activity sites for reaction might largely increase the catalytic current density and decrease overpotentials as well as Tafel slopes. Controlling the coordination numbers and adjusting the elemental species coordinated with metal atoms can change the electron structure of metal configurations, which are responsible for the activity and stability of SACs. In practical applications, the bifunctional catalysts with good performances for both OER and ORR are more desirable. Despite

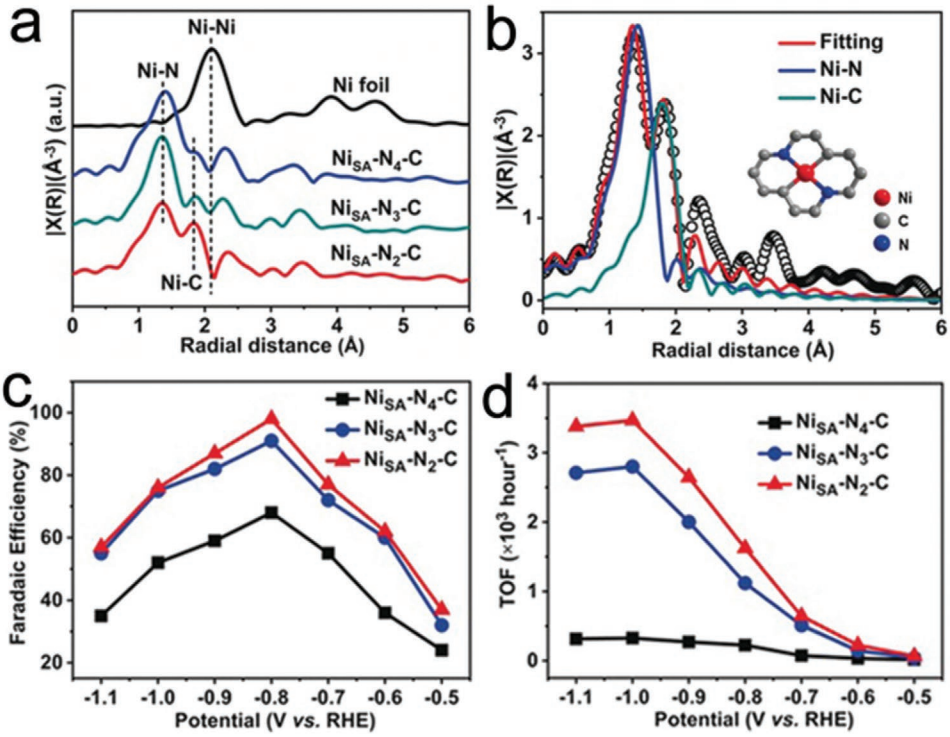

Figure 13. a) FT-EXAFS spectra of Ni_{SA}–N_x–C and Ni foil; b) EXAFS fitting results for Ni_{SA}–N_2–C; c) FEs of CO at different applied potentials; d) the corresponding TOFs of CO production on Ni_{SA}–N_x–C. Reproduced with permission.[58] Copyright 2020, Wiley-VCH.

great efforts and progress made in the past few years, there is still a long way to go on the synthesis of high-performance catalysts and widespread application of economically efficient catalysts in overall water splitting.

4.4. CO_2 Reduction Reaction

Converting CO_2 into various energy sources such as CO, ethanol, methanol, methane, and formic acid is an attractive strategy to achieve the carbon neutral economic and solve the energy issues. How to increase current densities and maintain the high Faradaic efficiency (FE) during electrochemical reduction of CO_2 is essential for the real application of CO_2RR.

Electroreducing CO_2 into CO has been regarded as potential pathway for CO_2 storage and conversion. Generally, the production of CO from electroreducing CO_2 basically contains three steps:[33b] 1) $CO_2 + H^+ + e^- \rightarrow COOH^*$; 2) $COOH^* + H^+ + e^- \rightarrow CO^* + H_2O$; 3) $CO^* \rightarrow CO + *$. Thus, the formation and dissociation of COOH* on catalytic active sites are of vital importance. Attributed to the high-density of low-coordinated metal sites, SACs show superior catalytic performances to reduce CO_2 to CO, with boosting activity, excellent selectivity, and ultrahigh FE. As a noble-metal-free catalyst, Ni-based SACs with individual Ni atoms coordinated with N embedded on carbon supports are efficiency for the electrocatalytic CO_2 to CO. For example, Yan et al. reported a kind of coordinatively unsaturated Ni–N sites doped on porous carbon through the pyrolysis of Zn/Ni bimetallic ZIF-8,[84] which had a Ni loading as large as 5.44 wt%. The resulting Ni single atoms decorated on carbon composites exhibited extraordinary catalytic activities for CO_2RR. The current density for CO production increases with the overpotential, reaching a value of about 71.5 mA cm^{-2} at –1.03 V. What's more, a high CO FE of 92.0–98.0% was maintained when measured under potentials ranging from –0.53 to –1.03 V. It is demonstrated that the unsaturated coordinating bonds of Ni–N sites are responsible for the high activity during the catalytic process, which makes the CO_2RR taking place more easily than the HER. In another work, through the one-step pyrolysis of ZIF-8 implanted with Ni ions based on a double-solvent method, atomically dispersed Ni atoms anchoring on N-doped porous carbon have been prepared.[53b] The HAADF-STEM and XAFS characterizations indicated that each Ni atom in the samples was coordinated by three N atoms, serving as the metal centers for selective reduction of CO_2 to CO under a proper condition. The catalysts showed a boosting performance with a high TOF of 5273 h^{-1} and a FE above 71.9% at the overpotential of 0.89 V.

Very recently, Jiang and co-workers synthesized a Ni_{SA}–N_x–C with different N coordination numbers by controlling the pyrolysis temperature of PPy@MgNi-MOF-74 composite.[58] Single Ni atoms decorated on carbon supports via Ni—N bonds with coordination number from 4 to 2 are strategically developed (**Figure 13**a,b). The Ni–N coordination environment showed a great influence on the catalytic performance for CO_2 to CO. The Ni_{SA}–N_2–C with a low-coordination number exhibited a superior electrocatalytic activity than the Ni_{SA}–N_3–C and Ni_{SA}–N_4–C, achieving a high FE for CO with a turnover frequency as high as 1622 h^{-1} at 0.8 V (Figure 13c,d). DFT calculations suggested that the Ni–N_2 sites in Ni_{SA}–N_2–C facilitated the formation of

COOH*, which showed a desorption energy of 0.47 eV for CO releasing, much lower than the Ni_{SA}–N_3–C (1.03 eV) and Ni_{SA}–N_4–C (1.09 eV). The conclusion of low-coordinated metal–N active centers favoring the reduction of CO_2 to CO has also been demonstrated by other metals. In Wang's report, the bimetallic Co/Zn-ZIF-8-derived Co-SACs with a coordinating mode of Co–N_2 exhibited a higher activity and selectivity than Co–N_4 and Co–N_3 sites,[33b] which displayed a CO formation FE of 94% and a large current density of 18.1 mA cm^{-2} at the overpotential of 520 mV, as well as a record high TOF value of 18 200 h^{-1}. The better catalytic performance of Co–N_2 species is attributed to the fact that metal centers can acquire more unoccupied 3d orbitals when decreasing the coordinating bonds between N and Co, thus beneficial for the adsorption of $CO_2^{\bullet-}$ intermediates and accelerating the electroreduction of CO_2. However, in another work of their group, they found that the very high-coordinated metal centers exhibited a surprisingly high activity for CO_2 reduction.[85] The synthesized Co–N_5 sites decorated on hollow porous carbons spheres showed a nearly 100% CO selectivity and outstanding stability. This indicates that the electronic structure of metals atoms is not the only factor affecting the activities of SACs, and other atoms near the metal centers may also contribute to the enhancement of electrocatalytic performances. Thus, insights into the coordination environment of metal atoms and revealing the real active sites for CO_2RR are urgently needed. On this side, Pan et al. prepared and studied the catalytic performance of Fe–N_4–C and Co–N_4–C catalysts,[86] which revealed that the Fe is intrinsically more active than Co in M–N_4 for the production of CO from reducing CO_2. The Fe–N_4 coordination exhibited a larger current density, along with the highest FE for CO (93%) at the overpotential of 0.47 V and a superior thermodynamic suppression of HER. Theory calculations showed that the edge-hosted M–N_{2+2}–C_8 sites bridging two adjacent armchair-like graphitic layers were more active than the bulk-hosted M–N_{2+2}–C_{10} sites for the reduction of CO_2 to CO. This is because the carbon atom connected with N atom with dangling bonds near the metal center is another active center for the dissociation of COOH*, resulting in a better performance for CO_2RR. Sometimes, only one kind of metal centers in the catalysts is not enough for the efficient reduction of CO_2. Combining the advantages of different metal atoms is a good approach to improve the catalytic properties of SACs. In these catalysts, the exposed accessible active sites and synergistic effects between elements are responsible for the enhanced performances. For instance, Ni/Fe–N–C catalysts prepared by the carbonization of Fe- and Ni-doped ZIF-8 nanostructures have been demonstrated as efficient electrocatalysts for CO_2 reduction, which exhibited a maximum FE (98%) at −0.7 V for CO with an excellent durability.[87] The current density of Ni/Fe–N–C catalysts at −0.7 V is 7.4 mA cm^{-2}, which is 1.5 and 4.6 times higher than that of Ni–N–C and Fe–N–C, respectively. Additionally, this current density can reach 19.7 mA cm^{-2} at −1.0 V. The TOF value of Ni/Fe–N–C at −1.0 V is 7682 h^{-1}, much larger than Ni–N–C and Fe–N–C. When introducing Fe into the catalysts, the Fe/Ni–N bimetal sites would undergo a structural change into a CO-adsorbed moiety upon CO_2 uptake, which will significantly improve the kinetic of reaction by decreasing the energy barrier. Theoretical calculations reveal that Fe–Ni centers are first passivated by strongly bonded CO*, providing an additional active sites for the second CO_2 activation either on Fe or Ni. Then, the reduction of CO_2 occurs on Fe sites, resulting in a lower reaction barrier for CO_2RR than simplex Fe or Ni centers.

It should be noted that the structure of catalysts such as sizes, pores, and surface areas also plays an important role during the catalytic process. Benefiting from the interconnected porous structure with a large active surface area that favors the transportation of reactant, the 3D net-like CoSA/HCNFs could achieve a 91% FE for CO with a current density of 67 mA cm^{-2} in a typical H-type cell,[19b] and the self-supported single-atom Ni-immobilized porous carbon membrane (NiSA/PCFM) catalysts showed a current density of 308.4 mA cm^{-2} for CO with a good FE of 88% even tested for 120 h.[19d] Engineering construction of mesopores in catalysts is another approach for improving the catalytic performance of SACs. By means of the introduction of large mesopores into ZIF-derived carbons, Fe single atoms immobilized on the mesoporous carbon framework not only show an excellent ORR activity but also display a good performance for CO reduction.[47a] Very recently, the rare earth-based SACs, in which the metal centers are coordinated with six nitrogen atoms located on the large-sized carbon defects, displayed an efficient catalytic activity for CO_2RR at ambient conditions.[20]

Electrocatalytic reduction CO_2 into multicarbon products such as alcohol, acetone, or acid is highly desirable, while it faces a big challenge. Among various kinds of catalysts, the Cu-based catalysts are proved to be efficiency for the conversion of CO_2 into high-value products.[88] This may be attributed to the fact that Cu sites can further reduce CO intermediates with an optimal binding energy and result in the C–C coupling. However, particle-like electrocatalytsts usually produce a broad mix of gaseous and liquid phase chemicals, owing to the different selectivities on various lattice planes or defects of polycrystalline Cu-based NPs. Thus, developing an economic efficiency catalyst with a good selectivity for high-value products from CO_2 is very important. Many studies demonstrated that single-metal catalysts showed a great potential for the reduction of CO_2 to high-value products with good selectivity and stability. For instance, single Fe sites on N-doped carbons showed a good catalytic performance for the reduction of CO_2 to CH_3COOH at a very-low potential.[89] The atomic cobalt layers with partially oxidized Co sites are more active for reducing CO_2 to HCOOH than the pure atomic cobalt layer catalysts, showing negligible decay in current density with a high FE of about 90% after tested for 40 h.[90]

Based on the electrospinning method with a following pyrolysis process, the atomically dispersed Cu atoms located on the through-hole carbon nanofibers (CuSAs/TCNFs) were fabricated by He and co-workers (**Figure 14**a).[57] Benefiting from the favorable mechanical strength and flexibility of carbon membrane, the obtained catalysts that combined the gas-diffusion and catalyst layers into a single structure could be directly used as a cathode for CO_2 reduction. EXAFS results revealed the Cu–N_4 configurations of the catalysts (Figure 14b,c). The CuSAs/TCNFs showed a good performance for CO_2RR (Figure 14d), and only C1 chemicals (CH_3OH and CO) were detected, which might be attributed to the through-hole structures and synergistic effects between Cu, N, and C species. The mixture

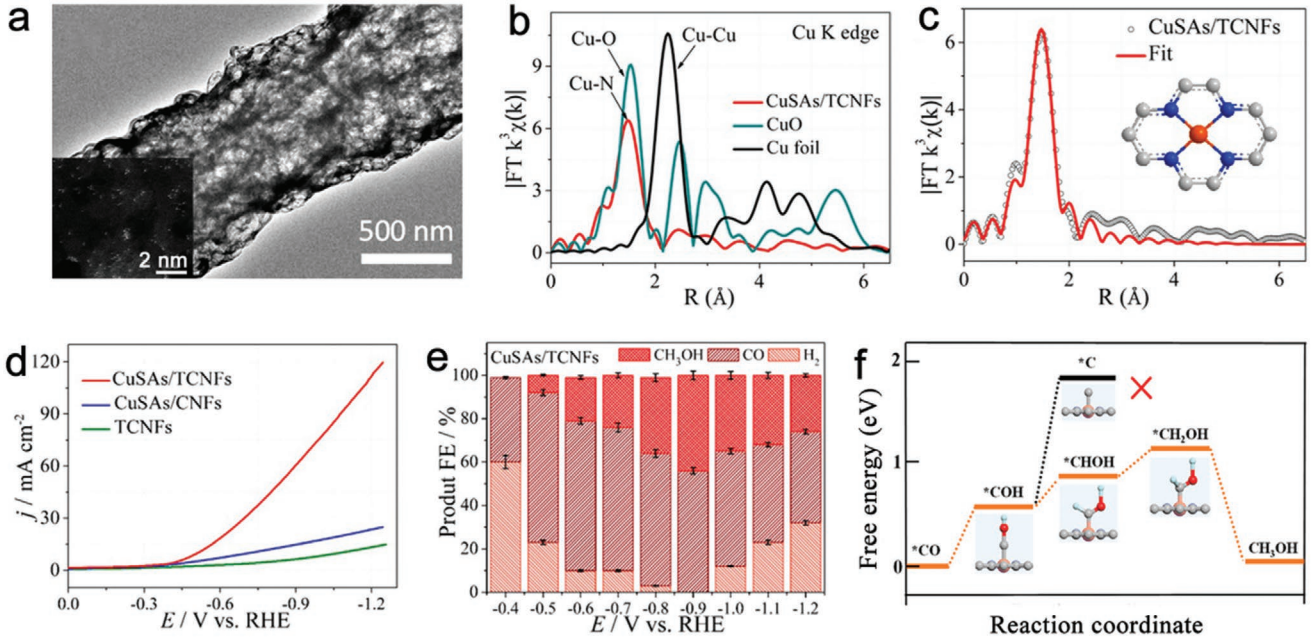

Figure 14. a) TEM images for CuSAs/TCNFs; b) FT k^3-weighted EXAFS spectra; c) fitting EXAFS data for CuSAs/TCNFs; d) LSV curves of tested catalysts in CO_2 saturated 0.1 M $KHCO_3$; e) FEs of all products on CuSAs/TCNFs. f) Free energies for the conversion of *CO to CH_3OH on Cu–N_4 structure. Reproduced with permission.[57] Copyright 2019, American Chemical Society.

production of gas- and liquid-phase at –0.9 V was composed of 56% CO and 44% nearly pure methanol (Figure 14e). In addition, the CuSAs/TCNFs could retain a steady current density of about 90 mA cm^{-2} with negligible declination after 50 h at –0.9 V, and showed no change in morphologies and compositions. It should be mentioned that the CuSAs/TCNFs membrane-like self-supporting electrode shows potential applications in electrocatalysis with industrial productions. To have more insights into the catalysis process from CO_2 to methanol, theory calculations based on DFT methods have been applied. It is found that the reduction of COH* intermediates into CHOH* on Cu–N_4 sites is more easy than the formation of C*, which is the key step for CH_4 production (Figure 14f). Thus, the reaction steps for generating CH_3OH on Cu–N_4 active sites are like this: $CO_2 \rightarrow$ *COOH $\rightarrow$ *CO $\rightarrow$ *COH $\rightarrow$ *CHOH $\rightarrow$ *CH_2OH $\rightarrow$ CH_3OH. This pathway has also been predicted by the first-principle calculations in a model of Cu-based single-atom alloys.[91] Apart from methanol, acetone can also be produced from the reduction of CO_2 by properly designing the metal sites and coordination environments of catalysts. Zhao et al. reported a single Cu decorated on N-doped porous carbon (Cu-SA/NPC) catalyst through the carbonization of Cu-doped ZIF-8 in nitrogen atmosphere.[19c] When used as the eletrocatalysts for CO_2 reduction, the major product in the reaction is identified to be acetone, showing a production rate of 336.1 μg h^{-1} with a FE of 36.7%. The DFT calculations suggest that the Cu metal sites coordinated with four pyrrole-N atoms are responsible for the production of acetone, which reduces the necessary reaction free energies for CO_2 reduction and C–C coupling.

It is worth noting that SACs for electroreduction of CO_2 is still in an initial stage despite some achievements made in this field (**Table 2**). The products of the reaction are intricate, and reaction mechanisms are not clear yet. Due to the existence of CO or its relative intermediates during the catalysis process, which easily absorbed on single-metal atoms and poison the catalysts, the durability of SACs is a major problem. Additionally, how to increase the FE of the productions, achieve the high current density of the reaction, and keep the high activity and selectivity of catalysts still need further investigations.

4.5. Nitrogen Reduction Reaction

Comparing to the NRR in industry, usually taking place under a high pressure and high temperature, the electrochemical N_2 into NH_3 at room temperature has many advantages and attracts rapidly increasing attention in recent years. Although significant efforts have been paid on this filed, the electrocatalysis N_2 into NH_3 still suffers from many problems, such as a large overpotential, a relatively low FE, and a slow N_2 adsorption kinetics as well as the sluggish cleavage of N≡N triple bonds, resulting in a low yield of NH_3.[92] As a competing reaction during NRR, the HER is easy to take place because of the lower theoretical limiting potential for H_2 generation than NH_3 formation. Most protons and electrons tend to form H_2 rather than NH_3, which is the main challenge that hinders the production of NH_3 from N_2 under ambient conditions. Thus, increasing the activity and selectivity of the electrocatalysts is of importance for the development of NRR.

For electrocatalytic reducing N_2 to NH_3 on heterogeneous catalysts, two fundamental mechanisms named dissociative and associative pathway have been proposed (**Figure 15**a).[93] In the dissociative process, N_2 molecules absorbed on the surface

Table 2. Summary of SACs derived from MOF precursors for CO_2 reduction reaction.

Catalyst	MOF precursor	Metal configuration	Metal content	Electrolyte	Product	Performance				Refs.
						j [mA cm^{-2}]	FE [%]	TOF [h^{-1}]	Stability	
CoSA/HCNFs	Co-ZIF-8/PAN	Co–N_4	0.7 wt%	0.1 M $KHCO_3$	CO	67 (–0.9 V)	91 (–0.9 V)	–	Negligible degradation of current density for 50 h	[19b]
NiSA/PCFM	Ni-ZIF-8/PAN	Ni–N_4	1.3 wt%	0.5 M $KHCO_3$	CO	56.1 (–1.0 V)	96 (–0.7 V)	–	Retaining more than 95% of initial value after 120 h	[19d]
NiSA–N_2–C	PPy@MgNi-MOF-74	Ni–N_2–C_2	0.9 wt%	0.5 M $KHCO_3$	CO	–	98 (–0.8 V)	1622 (–0.8 V)	Nearly unchanged current density and FE for CO production after 10 h at –0.8 V	[58]
FeSAs/CNF-900	$Zn_{10}Fe_1$-ZIF	Fe–N_x	4.58 wt%	0.5 M $KHCO_3$	CO	2.9 (–0.47 V)	86.9 (–0.47 V)	639.9 (–0.77 V)	A slight decay of current density after 12 h at –0.47 V	[47a]
Cu-SA/NPC	Cu-doped ZIF-8	Cu–N_4	0.59 wt%	0.1 M $KHCO_3$	Acetone and CO	–	36.7 for acetone (–0.36 V)	–	FE for acetone remained at ≈36.7% for 5 cycles	[19c]
NiSAs/NCNTs	ZIF-8/DCD/Ni^{2+}	–	6.63 wt%	0.5 M $KHCO_3$	CO	41.5 (–0.9 V)	97 (–0.9 V)	1176 (–1.0 V)	Little decay during 30 h of operation	[34b]
CuSAs/TCNFs	Cu-ZIF-8/PAN	Cu–N_4	1.3 wt%	0.5 M $KHCO_3$	CH_3OH and CO	93 for CH_3OH (–0.9 V)	44 and 56 (–0.9 V)	–	More than 50 h stability	[57]
Ni/Fe–N–C	NiFe-ZIF-8	(Ni,Fe)–N_6	Ni: 0.97 wt% Fe: 0.34 wt%	0.5 M $KHCO_3$	CO	9.5 (–0.7 V)	98 (–0.7 V)	7682 (–1.0 V)	Maintaining 99% of FE for CO after 30 h	[87]
SE-Ni SAs@PNC	Ni NPs@NC	–	–	0.5 M $KHCO_3$	CO	18.3 (–1.0 V)	87.8 (–1.0 V)	47 805 (–1.0 V)	No obvious decay for 60 h at –1.0 V	[34a]
C-Zn_1Ni_4 ZIF-8	Zn_xNi_y ZIF-8	Ni–N_x	5.44 wt%	0.5 M $KHCO_3$	CO	22 (–0.83 V)	98 (–0.83 V)	≈10 087 (–1.13 V)	Showing a CO FE of 97.8% at –0.63 V for 720 min	[84]
Fe–N–C	Fe-ZIF-8	Fe–N_{2+2}–C_8	0.1 at%	0.1 M $KHCO_3$	CO	–	93 (–0.58 V)	–	Giving the FE for CO >93% after 20 h	[85]
Ni SAs/N–C	Ni@ZIF-8	Ni–N_3C	1.53 wt%	0.5 M $KHCO_3$	CO	7.37 (–1.0 V)	71.9 (–0.9 V)	5273 (–1.0 V)	No obvious decay in FE and current density for 60 h	[53b]
Co–N_2	Co-ZIF	Co–N_2–C	0.25 wt%	0.5 M $KHCO_3$	CO	18.1 (–0.63 V)	94 (–0.63 V)	18 200 (–0.63 V)	Negligible decay in current density and FE for 60 h at –0.63 V	[33b]

of catalysts first undergo the cleavage of N≡N triple bond before the hydrogenation process, which need high energy to overcome the large activation barrier. In terms of associative mechanism, two N atoms of the adsorbed N_2 are bonded together during the hydrogenation process and the N—N bond is cleaved with the release of the first NH_3 molecule. According to the difference of hydrogenation process, the associative mechanism can be divided into two pathways including distal and alternating pathway. It is considered that, in distal pathway, the distal N atom far away from the end-on adsorption site is preferentially hydrogenated until releasing the first NH_3 molecule, and the second NH_3 are formed by a following repeat process. In contrast, two N atoms are hydrogenated alternately with the proton-coupled electron transfer during the alternating pathway, and two NH_3 molecules are released sequentially at the final step.

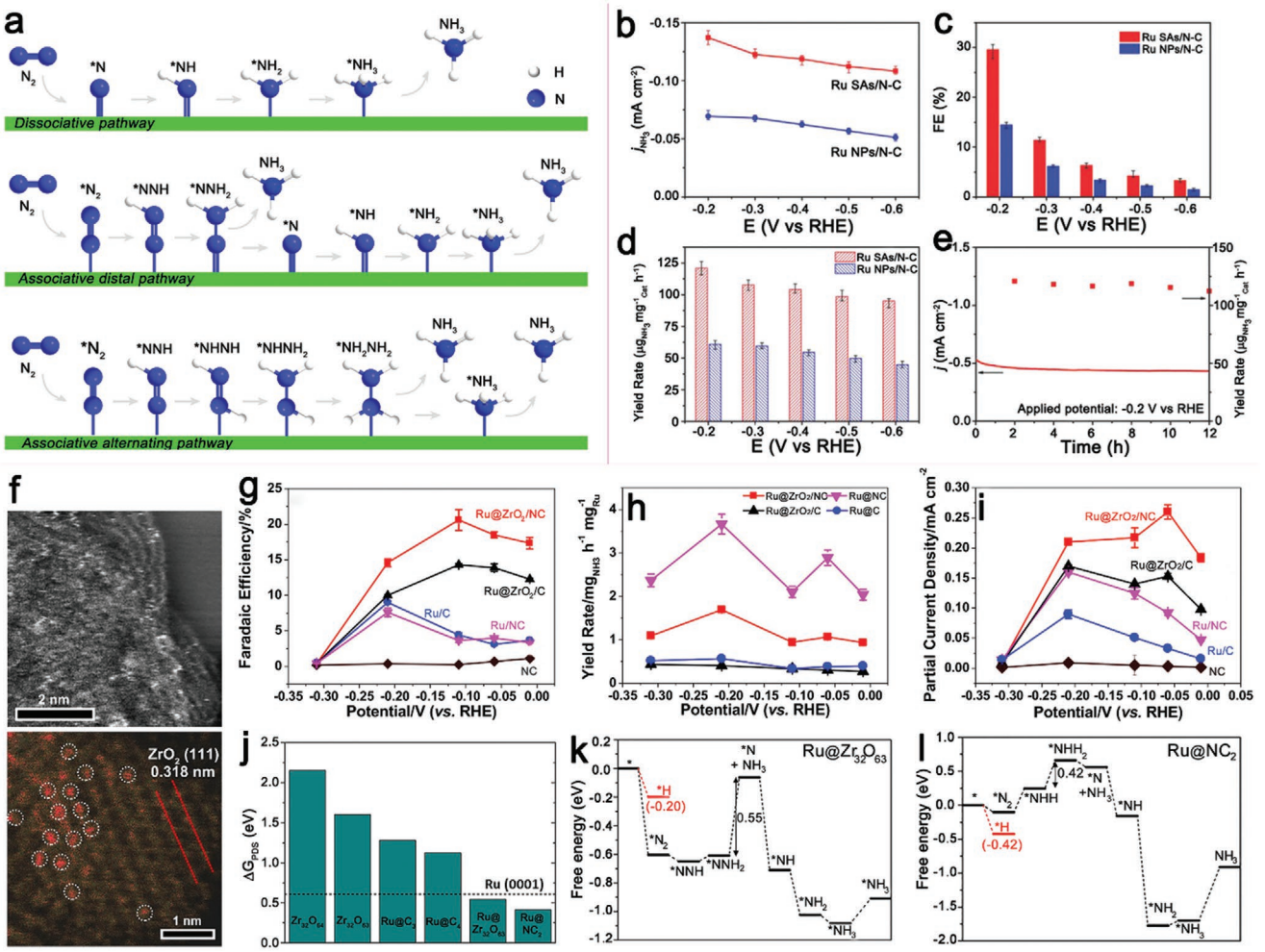

Figure 15. a) Schematic illustrations of mechanisms (dissociative and associative pathway) for NRR. Reproduced with permission.[93a] Copyright 2014, Royal Society of Chemistry. b) Current densities for NH_3 production; c) FEs and d) yield rate of NH_3 at different potentials on Ru SAs/N–C and Ru NPs/N–C; e) durability test for Ru SAs/N–C at –0.2 V versus RHE. Reproduced with permission.[95b] Copyright 2018, Wiley-VCH. f) HAADF-STEM images for Ru@ZrO_2/NC catalysts; g) the FEs, h) yield rates, and i) partial current densities of NH_3 over Ru-related single-atom catalysts at various applied potentials; j) ΔG_{PDS} for NRR on various reaction sites; k,l) free energy diagram for NRR over Ru@$Zr_{32}O_{63}$ and Ru@NC_2, respectively. Reproduced with permission.[95c] Copyright 2019, Cell Press.

In the past few years, a variety of electrocatalysts including noble or non-noble metal-based catalysts and metal-free catalysts have been applied for reducing N_2 to NH_3 at ambient conditions.[94] The reaction efficiency can be greatly improved by using single-atom catalysts.[95] Zeng and co-workers reported a kind of isolated Ru single atoms supported on a ZIF-8-derived carbon.[95b] As shown in Figure 15b–e, Ru-SACs can get an FE of 29.6% for NH_3 production with the partial current density of 0.13 mA cm^{-2}. This catalyst shows a yield rate as high as 120.9 μg_{NH3} h^{-1} mg_{cat}^{-1}, which is one order of magnitude higher than most reported catalysts. To deeply understand the reaction mechanism, the Gibbs free energy (ΔG) for each step involved N_2 reduction on Ru_1–N_3, Ru_1–N_4 and Ru(101) have been calculated. The variation in ΔG from *NNH to *NNH_2 is more negative than that from *NNH to *NHNH, suggesting the distal pathway for N_2 reduction on Ru-SACs. From the reaction process, N_2 dissociation is the rate-limiting step as which exhibits the highest energy barrier among all steps. The ΔG for N_2 dissociation on Ru_1–N_3 and Ru_1–N_4 are 0.73 and 0.74, respectively, lower than that of 0.91 eV for Ru(101), demonstrating the superior NRR performances of Ru-SACs.

Though the SACs can significantly improve the catalytic activity for NRR, the competing reaction of HER should be suppressed to enhance the yields and FE for N_2 reduction. Comparing to Ru NPs, single Ru atoms decorated on UiO-66-derived N-containing carbon supports showed a superior electrocatalytic performance for NRR in aqueous electrolyte, with a yield rate of 3.665 mg_{NH3} h^{-1} mg_{Ru}^{-1} for NH_3 at –0.21 V (vs RHE) (Figure 15f–i).[95c] It was found that the ZrO_2 in carbon supports would suppress the HER and showed little effects on NH_3 yield rate, affording a maximum ammonia FE as high as 21% at –0.11 V with an overpotential of 0.17 V. DFT calculations suggested that Ru@NC_2 species are the major active centers for reducing N_2 to NH_3 with a high yield rate, while the Ru sites combined with oxygen vacancies are responsible for the improved selectivity owing to their advantages in stabilization

of *NNH, destabilization of *H, and enhancing adsorption of N_2 (Figure 15j–l).

In most cases of N_2 to NH_3, SACs are attractive in acidic or alkaline media, while the catalytic performances in neutral media are less considered. In addition, it is highly desirable for the development of non-noble metal catalysts for NRR. As a typical coordination mode in SACs, Fe–N_4 configurations exhibited comparable or even superior ORR catalytic activity to Pt-based catalysts, while they are rarely studied in NRR attributed to their relatively low activity than noble metal catalysts. Recently, Liu and co-workers investigated the NRR performances of Fe single sites supported on N-doped porous carbons derived from a bimetallic FeZn-MOF, which exhibited a good NRR in neutral media (0.1 M phosphate buffer solution).[95e] The synthesized catalysts showed a high FE of 18.6 ± 0.8% for NH_3 with the yield of 62.9 ± 2.7 μg_{NH3} h^{-1} mg_{cat}^{-1} at –0.4 V (vs RHE).

4.6. Other Electrochemical Reactions

At present, although SACs are widely studied in a variety of fields, such as photocatalysis,[28b,49] organic synthesis,[30–31,96] and so on, most MOF-derived SACs are mainly focused on electrochemical applications in ORR and CO_2RR, and their applications on water splitting and NRR are just at the initial stage. It was reported that single Rh atoms anchored on ZIF-8-derived N-doped carbon (SA-Rh/CN) exhibited a promising catalytic performance for formic acid oxidation.[61] The mass activity of 16.1 A mg^{-1} was obtained at the peak potential, which is ≈28, 67, and 805 times larger than the values found for Pd/C (0.57 A mg^{-1}), Pt/C (0.24 A mg^{-1}), and Rh/C (0.02 A mg^{-1}), respectively. Attributed to the high barrier for CO generation and the unfavorable binding with CO on SA-Rh/CN, the single-metal catalysts exhibited excellent stability and CO tolerance, which is of great importance for the practical application in fuel cells.

5. Conclusions and Perspectives

Benefiting from the advantages in low-coordinating environment, unique active centers, and maximum utilization of metal atoms, SACs are considered as an ideal candidate to inherit the merits of heterogeneous and homogeneous catalysts. Therefore, developing a reasonable strategy to synthesize high-quality SACs is significant for their practical applications. MOFs with atomically dispersed metal atoms/clusters, well defined pore structures, ultrahigh specific surface areas, and pore volumes have recently emerged as an attractive platform to construct SACs with highly dispersed metal sites. Compared with other approaches for SACs, MOF-derived SACs show the following advantages: 1) plentiful organic linkers with adjustable functional groups provide an ideal access for heteroatoms such as N, P doping on carbon supports after carbonization, which will act as the coordination sites for anchoring single-metal atoms; 2) the high percentage of metal species with facile controllability in MOFs are beneficial for the dispersion of metal atoms and prevent their aggregations during pyrolysis, providing a feasible approach to design single- or dual-atom catalysts with high loading of metals; 3) the uniform pore structure favors the encapsulation of guest molecules, and thus facilitating the preparation of SACs with various functionalities; 4) MOF-derived carbon supports usually have ultrahigh specific surface areas and large porosity as well as 3D interconnected pore structure, which largely expose the density of metal active sites and lead to an excellent catalytic performance.

In this review, we have summarized the recent progress on MOF-derived SACs from the synthesis strategies including the pyrolysis of pristine MOFs and MOF composites or mixtures, advanced characterization techniques and electrochemical applications such as ORR, OER, HER, CO_2RR, NRR, etc. It can be concluded that MOF-derived SACs not only display excellent electrocatalytic activity along with superior electronic conductivity and thermal and chemical stability, but also provide an ideal platform to reveal the reaction mechanism and pathways in energy-related electrocatalysis. Despite tremendous progress achieved in MOF-derived SACs, challenges in this field still need to be overcome in order to get a more active and economic efficient catalyst in practical applications.

I) To improve the catalytic activity of SACs, the precise control on the density of active sites and coordination environment of metal centers should give priority consideration. In terms of synthesis process, increasing the metal loading of catalysts is the most efficient approach to enhance the density of active sites, while metal atoms tend to aggregate into metal NPs or nanoclusters at high pyrolysis temperatures if the target metals are too much in MOF precursors. Thus, finding a suitable MOF precursor to yield carbon supports with rich anchoring sites and large specific surface areas to prevent the aggregation of metal atoms is necessary. Sometimes, the fabricated single-metal atoms are usually located on both outer and inner surface of MOF-derived carbons. These inner-located metal sites are hard to be utilized during the electrocatalytic process. Therefore, designing the MOF-derived carbon supports into hierarchically porous structures or 3D interconnected structures is also a good strategy to achieve SACs with highly exposed metal active sites, which would significantly enhance the utilization of metal atoms. In addition, the coordination environment of metal centers shows a great contribution to their intrinsic activity, which can be improved by tuning the electronic structure of metal sites via heteroatoms doping (such as N, P, S) or engineering the metal centers into unsaturated coordination configuration. Heteroatoms in supports usually result in the formation of defects and affect the catalytic activity of metal atoms by synergetic effects, which contribute greatly to the enhancement of activity. Furthermore, adjusting the pyrolysis temperature might be also an efficient pathway to control the coordinating structures of metal centers.

II) Developing a facile and low-cost strategy to largely produce SACs from MOF is of significant importance from the viewpoint of practical applications. To date, only limited kinds of MOFs, such as ZIF-8, ZIF-67, (Zn)MOF-74, UiO-66-NH_2, and MIL-101-NH_2, have been well-investigated as precursors to synthesize SACs despite thousands of MOFs being reported. Apart from the acceptable cost of ZIFs, most MOFs are very

expensive and difficult for the scalable production, which is one of the biggest challenges for industrial application of MOF-derived SACs at present. Fortunately, with the development of synthesis techniques, more and more economic ligands will be applied in MOF science. Compared to the scarcity and irreversible noble-metal catalysts, MOF-derived SACs still show a bright future in catalysis field. In the following research, advanced synthesis strategies based on exploring economic-efficient MOF precursors and improving the yields of MOF-derived carbon catalysts are highly desirable.

III) Currently, most SACs are characterized by ex situ HAADF-STEM, XAFS, or IR spectroscopy, which are not able to fully understand their real roles in catalytic process. Indeed, the state of metal atoms in SACs will change depending on the reaction conditions such as temperature, pH values, and so on. Therefore, in situ characterization techniques including in situ HAADF-STEM, in situ XAS, and in situ IR spectroscopy are very useful tools to study the mechanisms of reactions taking placing on these heterogeneous catalysts. Though the use of in situ techniques to monitor the change of single-metal atoms during the reaction process is not widespread at present, more kinds of in situ characterization techniques will be applied on this field to deeply understand the reactive intermediates, real active sites, and reaction pathways in the near future. In case of electrocatalysis, the combination of theoretical computation (such as DFT) with in situ electrochemical techniques might provide some insights into the contributions of SACs during the reaction process, and thus inspiring us to design and fabricate more high-performance SACs.

IV) As a newly emerged research topic, most researches about MOF-derived SACs are focused on applications in ORR and CO_2RR, and only a few studies involve in HER, OER, and NRR. Their applications on general organic catalytic reactions, such as the activation of C–H, hydrogenative coupling of nitroarenes, and hydrogenation and hydrodeoxygenation of biomass molecule, are rarely found. In the future, a broad application of SACs on energy-related catalysis or general organic synthesis are encouraged to be explored.

In summary, by virtue of MOF-templated strategy, various kinds of single-metal atoms decorated on porous carbon supports with controllable morphologies and elemental functionalities can be achieved. These MOF-derived high-performance SACs show great potential applications in a variety of electrochemical reactions. Continued research effort should be paid on the comprehensive understanding of the formation of SACs and their real roles in catalytic reactions. Moreover, pushing on the industrial application of SACs is another significant aspect that needs to be achieved.

Acknowledgements

The authors thank the editors for the kind invitation, the reviewers for valuable suggestions, and AIST for the financial support.

Conflict of Interest

The authors declare no conflict of interest.

Keywords

carbon nanostructures, electrocatalysis, metal–organic frameworks, single-atom catalysts

Received: August 7, 2020
Revised: September 18, 2020
Published online:

[1] a) Z. Li, Q. Xu, *Acc. Chem. Res.* **2017**, *50*, 1449; b) L. Liu, A. Corma, *Chem. Rev.* **2018**, *118*, 4981; c) X. Yang, J.-K. Sun, M. Kitta, H. Pang, Q. Xu, *Nat. Catal.* **2018**, *1*, 214.
[2] a) Y. Chen, Q.-L. Zhu, N. Tsumori, Q. Xu, *J. Am. Chem. Soc.* **2015**, *137*, 106; b) Q.-L. Zhu, J. Li, Q. Xu, *J. Am. Chem. Soc.* **2013**, *135*, 10210; c) Q. Wang, N. Tsumori, M. Kitta, Q. Xu, *ACS Catal.* **2018**, *8*, 12041.
[3] M. Crespo-Quesada, A. Yarulin, M. Jin, Y. Xia, L. Kiwi-Minsker, *J. Am. Chem. Soc.* **2011**, *133*, 12787.
[4] a) Q. Wang, L. Chen, Z. Liu, N. Tsumori, M. Kitta, Q. Xu, *Adv. Funct. Mater.* **2019**, *29*, 1903341; b) L. Zou, M. Kitta, J. Hong, K. Suenaga, N. Tsumori, Z. Liu, Q. Xu, *Adv. Mater.* **2019**, *31*, 1900440.
[5] a) X.-F. Yang, A. Wang, B. Qiao, J. Li, J. Liu, T. Zhang, *Acc. Chem. Res.* **2013**, *46*, 1740; b) Y. Wang, J. Mao, X. Meng, L. Yu, D. Deng, X. Bao, *Chem. Rev.* **2018**, *119*, 1806.
[6] a) C.-C. Hou, H.-F. Wang, C. Li, Q. Xu, *Energy Environ. Sci.* **2020**, *13*, 1658; b) Y.-S. Wei, M. Zhang, R. Zou, Q. Xu, *Chem. Rev.* **2020**, *120*, 12089; c) C. Lu, R. Fang, X. Chen, *Adv. Mater.* **2020**, *32*, 1906548; d) Y. Chen, S. Ji, C. Chen, Q. Peng, D. Wang, Y. Li, *Joule* **2018**, *2*, 1242; e) Y. Zhao, T. Ling, S. Chen, B. Jin, A. Vasileff, Y. Jiao, L. Song, J. Luo, S.-Z. Qiao, *Angew. Chem., Int. Ed.* **2019**, *58*, 12252; f) T. Wang, Q. Wang, Y. Wang, Y. Da, W. Zhou, Y. Shao, D. Li, S. Zhan, J. Yuan, H. Wang, *Angew. Chem., Int. Ed.* **2019**, *58*, 13466.
[7] a) C. C. Hou, L. Zou, L. Sun, K. Zhang, Z. Liu, Y. Li, C. Li, R. Zou, J. Yu, Q. Xu, *Angew. Chem.* **2020**, *132*, 7454; b) C. Gao, J. Low, R. Long, T. Kong, J. Zhu, Y. Xiong, *Chem. Rev.* **2020**, *120*, 12175.
[8] C. Lecuyer, F. Quignard, A. Choplin, D. Olivier, J. M. Basset, *Angew. Chem., Int. Ed.* **1991**, *30*, 1660.
[9] T. Maschmeyer, F. Rey, G. Sankar, J. M. Thomas, *Nature* **1995**, *378*, 159.
[10] S. Abbet, A. Sanchez, U. Heiz, W.-D. Schneider, A. M. Ferrari, G. Pacchioni, N. Rösch, *J. Am. Chem. Soc.* **2000**, *122*, 3453.
[11] T. Kobayashi, *Catal. Today* **2001**, *71*, 69.
[12] S. F. Hackett, R. M. Brydson, M. H. Gass, I. Harvey, A. D. Newman, K. Wilson, A. F. Lee, *Angew. Chem.* **2007**, *119*, 8747.
[13] B. Qiao, A. Wang, X. Yang, L. F. Allard, Z. Jiang, Y. Cui, J. Liu, J. Li, T. Zhang, *Nat. Chem.* **2011**, *3*, 634.
[14] P. Yin, T. Yao, Y. Wu, L. Zheng, Y. Lin, W. Liu, H. Ju, J. Zhu, X. Hong, Z. Deng, G. Zhou, S. Wei, Y. Li, *Angew. Chem., Int. Ed.* **2016**, *55*, 10800.
[15] a) Y.-S. Wei, L. Sun, M. Wang, J. Hong, L. Zou, H. Liu, Y. Wang, M. Zhang, Z. Liu, Y. Li, S. Horike, K. Suenaga, Q. Xu, *Angew. Chem., Int. Ed.* **2020**, *59*, 16013; b) S. Zhu, J. Ge, C. Liu, W. Xing, *EnergyChem* **2019**, *1*, 100018.
[16] a) Y. Yang, K. Mao, S. Gao, H. Huang, G. Xia, Z. Lin, P. Jiang, C. Wang, H. Wang, Q. Chen, *Adv. Mater.* **2018**, *30*, 1801732; b) Z. Kou, W. Zang, Y. Ma, Z. Pan, S. Mu, X. Gao, B. Tang, M. Xiong, X. Zhao, A. K. Cheetham, L. Zheng, J. Wang, *Nano Energy* **2020**, *67*, 104288.
[17] R. Zhao, Z. Liang, S. Gao, C. Yang, B. Zhu, J. Zhao, C. Qu, R. Zou, Q. Xu, *Angew. Chem.* **2019**, *131*, 1997.
[18] Z. Pu, I. S. Amiinu, R. Cheng, P. Wang, C. Zhang, S. Mu, W. Zhao, F. Su, G. Zhang, S. Liao, S. Sun, *Nano-Micro Lett.* **2020**, *12*, 21.

[19] a) Z. Wang, J. Yang, J. Cao, W. Chen, G. Wang, F. Liao, X. Zhou, F. Zhou, R. Li, Z.-Q. Yu, G. Zhang, X. Duan, Y. Wu, *ACS Nano* **2020**, *14*, 6164; b) H. Yang, Q. Lin, Y. Wu, G. Li, Q. Hu, X. Chai, X. Ren, Q. Zhang, J. Liu, C. He, *Nano Energy* **2020**, *70*, 104454; c) K. Zhao, X. Nie, H. Wang, S. Chen, X. Quan, H. Yu, W. Choi, G. Zhang, B. Kim, J. G. Chen, *Nat. Commun.* **2020**, *11*, 2455; d) H. Yang, Q. Lin, C. Zhang, X. Yu, Z. Cheng, G. Li, Q. Hu, X. Ren, Q. Zhang, J. Liu, C. He, *Nat. Commun.* **2020**, *11*, 593.

[20] J. Liu, X. Kong, L. Zheng, X. Guo, X. Liu, J. Shui, *ACS Nano* **2020**, *14*, 1093.

[21] P. Liu, Y. Zhao, R. Qin, S. Mo, G. Chen, L. Gu, D. M. Chevrier, P. Zhang, Q. Guo, D. Zang, B. Wu, G. Fu, N. Zheng, *Science* **2016**, *352*, 797.

[22] a) S. An, G. Zhang, T. Wang, W. Zhang, K. Li, C. Song, J. T. Miller, S. Miao, J. Wang, X. Guo, *ACS Nano* **2018**, *12*, 9441; b) Y. Zheng, Y. Jiao, Y. Zhu, Q. Cai, A. Vasileff, L. H. Li, Y. Han, Y. Chen, S.-Z. Qiao, *J. Am. Chem. Soc.* **2017**, *139*, 3336; c) Y. Jiao, Y. Zheng, P. Chen, M. Jaroniec, S.-Z. Qiao, *J. Am. Chem. Soc.* **2017**, *139*, 18093.

[23] a) Y. Peng, B. Lu, S. Chen, *Adv. Mater.* **2018**, *30*, 1801995; b) M. B. Gawande, P. Fornasiero, R. Zbořil, *ACS Catal.* **2020**, *10*, 2231.

[24] D. Liu, J.-C. Li, S. Ding, Z. Lyu, S. Feng, H. Tian, C. Huyan, M. Xu, T. Li, D. Du, P. Liu, M. Shao, Y. Lin, *Small Methods* **2020**, *4*, 1900827.

[25] S. Ji, Y. Chen, X. Wang, Z. Zhang, D. Wang, Y. Li, *Chem. Rev.* **2020**, *120*, 11900.

[26] Y. Qu, Z. Li, W. Chen, Y. Lin, T. Yuan, Z. Yang, C. Zhao, J. Wang, C. Zhao, X. Wang, F. Zhou, Z. Zhuang, Y. Wu, Y. Li, *Nat. Catal.* **2018**, *1*, 781.

[27] a) Z. Zhang, C. Feng, C. Liu, M. Zuo, L. Qin, X. Yan, Y. Xing, H. Li, R. Si, S. Zhou, J. Zeng, *Nat. Commun.* **2020**, *11*, 1215; b) J.-C. Liu, H. Xiao, J. Li, *J. Am. Chem. Soc.* **2020**, *142*, 3375.

[28] a) Q. Liu, Y. Li, L. Zheng, J. Shang, X. Liu, R. Yu, J. Shui, *Adv. Energy Mater.* **2020**, *10*, 2000689; b) T. He, S. Chen, B. Ni, Y. Gong, Z. Wu, L. Song, L. Gu, W. Hu, X. Wang, *Angew. Chem., Int. Ed.* **2018**, *57*, 3493; c) H. Yan, Y. Lin, H. Wu, W. Zhang, Z. Sun, H. Cheng, W. Liu, C. Wang, J. Li, X. Huang, T. Yao, J. Yang, S. Wei, J. Lu, *Nat. Commun.* **2017**, *8*, 1070.

[29] T. Gan, Q. He, H. Zhang, H. Xiao, Y. Liu, Y. Zhang, X. He, H. Ji, *Chem. Eng. J.* **2020**, *389*, 124490.

[30] X. Wang, W. Chen, L. Zhang, T. Yao, W. Liu, Y. Lin, H. Ju, J. Dong, L. Zheng, W. Yan, X. Zheng, Z. Li, X. Wang, J. Yang, D. He, Y. Wang, Z. Deng, Y. Wu, Y. Li, *J. Am. Chem. Soc.* **2017**, *139*, 9419.

[31] Q. Yang, C. C. Yang, C. H. Lin, H. L. Jiang, *Angew. Chem.* **2019**, *131*, 3549.

[32] a) Y. Li, T. Yang, S. Qiu, W. Lin, J. Yan, S. Fan, Q. Zhou, *Chem. Eng. J.* **2020**, *389*, 124382; b) C.-X. Zhao, B.-Q. Li, J.-N. Liu, Q. Zhang, *Angew. Chem., Int. Ed.* **2020**, https://doi.org/10.1002/anie.202003917; c) Y. Chen, S. Ji, S. Zhao, W. Chen, J. Dong, W.-C. Cheong, R. Shen, X. Wen, L. Zheng, A. I. Rykov, S. Cai, H. Tang, Z. Zhuang, C. Chen, Q. Peng, D. Wang, Y. Li, *Nat. Commun.* **2018**, *9*, 5422; d) J. Li, L. Jiao, E. Wegener, L. L. Richard, E. Liu, A. Zitolo, M. T. Sougrati, S. Mukerjee, Z. Zhao, Y. Huang, F. Yang, S. Zhong, H. Xu, A. J. Kropf, F. Jaouen, D. J. Myers, Q. Jia, *J. Am. Chem. Soc.* **2020**, *142*, 1417; e) J. Li, H. Zhang, W. Samarakoon, W. Shan, D. A. Cullen, S. Karakalos, M. Chen, D. Gu, K. L. More, G. Wang, Z. Feng, Z. Wang, G. Wu, *Angew. Chem., Int. Ed.* **2019**, *58*, 18971.

[33] a) E. Jung, H. Shin, B.-H. Lee, V. Efremov, S. Lee, H. S. Lee, J. Kim, W. Hooch Antink, S. Park, K.-S. Lee, S.-P. Cho, J. S. Yoo, Y.-E. Sung, T. Hyeon, *Nat. Mater.* **2020**, *19*, 436; b) X. Wang, Z. Chen, X. Zhao, T. Yao, W. Chen, R. You, C. Zhao, G. Wu, J. Wang, W. Huang, J. Yang, X. Hong, S. Wei, Y. Wu, Y. Li, *Angew. Chem., Int. Ed.* **2018**, *57*, 1944.

[34] a) J. Yang, Z. Qiu, C. Zhao, W. Wei, W. Chen, Z. Li, Y. Qu, J. Dong, J. Luo, Z. Li, Y. Wu, *Angew. Chem., Int. Ed.* **2018**, *57*, 14095; b) P. Lu, Y. Yang, J. Yao, M. Wang, S. Dipazir, M. Yuan, J. Zhang, X. Wang, Z. Xie, G. Zhang, *Appl. Catal., B* **2019**, *241*, 113.

[35] J. Li, M. Chen, D. A. Cullen, S. Hwang, M. Wang, B. Li, K. Liu, S. Karakalos, M. Lucero, H. Zhang, C. Lei, H. Xu, G. E. Sterbinsky, Z. Feng, D. Su, K. L. More, G. Wang, Z. Wang, G. Wu, *Nat. Catal.* **2018**, *1*, 935.

[36] S. Ma, Z. Han, K. Leng, X. Liu, Y. Wang, Y. Qu, J. Bai, *Small* **2020**, *16*, 2001384.

[37] a) L. Jiao, H.-L. Jiang, *Chem* **2019**, *5*, 786; b) H. Xiang, W. Feng, Y. Chen, *Adv. Mater.* **2020**, *32*, 1905994.

[38] a) X. Xiao, L. Zou, H. Pang, Q. Xu, *Chem. Soc. Rev.* **2020**, *49*, 301; b) R. Fang, L. Chen, Z. Shen, Y. Li, *Catal. Today* **2020**, https://doi.org/10.1016/j.cattod.2020.03.019.

[39] a) Y. Wang, N.-Y. Huang, X.-W. Zhang, H. He, R.-K. Huang, Z.-M. Ye, Y. Li, D.-D. Zhou, P.-Q. Liao, X.-M. Chen, J.-P. Zhang, *Angew. Chem., Int. Ed.* **2019**, *58*, 7692; b) H. Li, L. Li, R.-B. Lin, W. Zhou, Z. Zhang, S. Xiang, B. Chen, *EnergyChem* **2019**, *1*, 100006; c) D.-D. Zhou, X.-W. Zhang, Z.-W. Mo, Y.-Z. Xu, X.-Y. Tian, Y. Li, X.-M. Chen, J.-P. Zhang, *EnergyChem* **2019**, *1*, 100016.

[40] a) N. Tsumori, L. Chen, Q. Wang, Q.-L. Zhu, M. Kitta, Q. Xu, *Chem* **2018**, *4*, 845; b) Y. Wang, N.-Y. Huang, J.-Q. Shen, P.-Q. Liao, X.-M. Chen, J.-P. Zhang, *J. Am. Chem. Soc.* **2018**, *140*, 38; c) D. Li, H.-Q. Xu, L. Jiao, H.-L. Jiang, *EnergyChem* **2019**, *1*, 100005.

[41] a) H.-F. Wang, L. Chen, H. Pang, S. Kaskel, Q. Xu, *Chem. Soc. Rev.* **2020**, *49*, 1414; b) Z. Liang, R. Zhao, T. Qiu, R. Zou, Q. Xu, *EnergyChem* **2019**, *1*, 100001; c) X. Li, X. Yang, H. Xue, H. Pang, Q. Xu, *EnergyChem* **2020**, *2*, 100027.

[42] a) L. Zou, Q. Xu, *Chem. - Asian J.* **2020**, *15*, 490; b) Y. Li, Y. Xu, W. Yang, W. Shen, H. Xue, H. Pang, *Small* **2018**, *14*, 1704435; c) B. Liu, X. Zhang, H. Shioyama, T. Mukai, T. Sakai, Q. Xu, *J. Power Sources* **2010**, *195*, 857.

[43] a) B. Liu, H. Shioyama, T. Akita, Q. Xu, *J. Am. Chem. Soc.* **2008**, *130*, 5390; b) L. Zou, C.-C. Hou, Q. Wang, Y.-S. Wei, Z. Liu, J.-S. Qin, H. Pang, Q. Xu, *Angew. Chem., Int. Ed.* **2020**, *59*, 19627; c) Z.-X. Li, B.-L. Yang, K.-Y. Zou, L. Kong, M.-L. Yue, H.-H. Duan, *Carbon* **2019**, *144*, 540.

[44] a) L. Cao, P. Dai, J. Tang, D. Li, R. Chen, D. Liu, X. Gu, L. Li, Y. Bando, Y. S. Ok, *J. Am. Chem. Soc.* **2020**, *142*, 8755; b) J. Cai, Y. Song, X. Chen, Z. Sun, Y. Yi, J. Sun, Q. Zhang, *J. Mater. Chem. A* **2020**, *8*, 1757.

[45] a) Y.-S. Wei, M. Zhang, M. Kitta, Z. Liu, S. Horike, Q. Xu, *J. Am. Chem. Soc.* **2019**, *141*, 7906; b) R. Wu, D. P. Wang, K. Zhou, N. Srikanth, J. Wei, Z. Chen, *J. Mater. Chem. A* **2016**, *4*, 13742.

[46] a) L. Zou, C.-C. Hou, Z. Liu, H. Pang, Q. Xu, *J. Am. Chem. Soc.* **2018**, *140*, 15393; b) C. C. Hou, L. Zou, Q. Xu, *Adv. Mater.* **2019**, *31*, 1904689; c) D. Zhu, F. Zheng, S. Xu, Y. Zhang, Q. Chen, *Dalton Trans.* **2015**, *44*, 16946.

[47] a) X. Chen, D.-D. Ma, B. Chen, K. Zhang, R. Zou, X.-T. Wu, Q.-L. Zhu, *Appl. Catal., B* **2020**, *267*, 118720; b) A. Han, B. Wang, A. Kumar, Y. Qin, J. Jin, X. Wang, C. Yang, B. Dong, Y. Jia, J. Liu, X. Sun, *Small Methods* **2019**, *3*, 1800471; c) H. Huang, K. Shen, F. Chen, Y. Li, *ACS Catal.* **2020**, *10*, 6579; d) M. Xiao, H. Zhang, Y. Chen, J. Zhu, L. Gao, Z. Jin, J. Ge, Z. Jiang, S. Chen, C. Liu, W. Xing, *Nano Energy* **2018**, *46*, 396.

[48] Q.-L. Zhu, W. Xia, L.-R. Zheng, R. Zou, Z. Liu, Q. Xu, *ACS Energy Lett.* **2017**, *2*, 504.

[49] X. Fang, Q. Shang, Y. Wang, L. Jiao, T. Yao, Y. Li, Q. Zhang, Y. Luo, H. L. Jiang, *Adv. Mater.* **2018**, *30*, 1705112.

[50] L. Fan, P. F. Liu, X. Yan, L. Gu, Z. Z. Yang, H. G. Yang, S. Qiu, X. Yao, *Nat. Commun.* **2016**, *7*, 10667.

[51] H. Zhang, S. Hwang, M. Wang, Z. Feng, S. Karakalos, L. Luo, Z. Qiao, X. Xie, C. Wang, D. Su, Y. Shao, G. Wu, *J. Am. Chem. Soc.* **2017**, *139*, 14143.

[52] Y. Chen, S. Ji, Y. Wang, J. Dong, W. Chen, Z. Li, R. Shen, L. Zheng, Z. Zhuang, D. Wang, Y. Li, *Angew. Chem., Int. Ed.* **2017**, *56*, 6937.

[53] a) R. C. Klet, T. C. Wang, L. E. Fernandez, D. G. Truhlar, J. T. Hupp, O. K. Farha, *Chem. Mater.* **2016**, *28*, 1213; b) C. Zhao, X. Dai, T. Yao, W. Chen, X. Wang, J. Wang, J. Yang, S. Wei, Y. Wu, Y. Li, *J. Am. Chem. Soc.* **2017**, *139*, 8078.
[54] L. Jiao, G. Wan, R. Zhang, H. Zhou, S. H. Yu, H. L. Jiang, *Angew. Chem., Int. Ed.* **2018**, *57*, 8525.
[55] W. Chen, J. Pei, C.-T. He, J. Wan, H. Ren, Y. Wang, J. Dong, K. Wu, W.-C. Cheong, J. Mao, X. Zheng, W. Yan, Z. Zhuang, C. Chen, Q. Peng, D. Wang, Y. Li, *Adv. Mater.* **2018**, *30*, 1800396.
[56] M. Xiao, J. Zhu, L. Ma, Z. Jin, J. Ge, X. Deng, Y. Hou, Q. He, J. Li, Q. Jia, S. Mukerjee, R. Yang, Z. Jiang, D. Su, C. Liu, W. Xing, *ACS Catal.* **2018**, *8*, 2824.
[57] H. Yang, Y. Wu, G. Li, Q. Lin, Q. Hu, Q. Zhang, J. Liu, C. He, *J. Am. Chem. Soc.* **2019**, *141*, 12717.
[58] Y.-N. Gong, L. Jiao, Y. Qian, C.-Y. Pan, L. Zheng, X. Cai, B. Liu, S.-H. Yu, H.-L. Jiang, *Angew. Chem., Int. Ed.* **2020**, *59*, 2705.
[59] L. Jiao, R. Zhang, G. Wan, W. Yang, X. Wan, H. Zhou, J. Shui, S.-H. Yu, H.-L. Jiang, *Nat. Commun.* **2020**, *11*, 2831.
[60] Y. He, S. Hwang, D. A. Cullen, M. A. Uddin, L. Langhorst, B. Li, S. Karakalos, A. J. Kropf, E. C. Wegener, J. Sokolowski, M. Chen, D. Myers, D. Su, K. L. More, G. Wang, S. Litster, G. Wu, *Energy Environ. Sci.* **2019**, *12*, 250.
[61] Y. Xiong, J. Dong, Z.-Q. Huang, P. Xin, W. Chen, Y. Wang, Z. Li, Z. Jin, W. Xing, Z. Zhuang, J. Ye, X. Wei, R. Cao, L. Gu, S. Sun, L. Zhuang, X. Chen, H. Yang, C. Chen, Q. Peng, C.-R. Chang, D. Wang, Y. Li, *Nat. Nanotechnol.* **2020**, *15*, 390.
[62] X. X. Wang, D. A. Cullen, Y.-T. Pan, S. Hwang, M. Wang, Z. Feng, J. Wang, M. H. Engelhard, H. Zhang, Y. He, Y. Shao, D. Su, K. L. More, J. S. Spendelow, G. Wu, *Adv. Mater.* **2018**, *30*, 1706758.
[63] D. Deng, X. Chen, L. Yu, X. Wu, Q. Liu, Y. Liu, H. Yang, H. Tian, Y. Hu, P. Du, R. Si, J. Wang, X. Cui, H. Li, J. Xiao, T. Xu, J. Deng, F. Yang, P. N. Duchesne, P. Zhang, J. Zhou, L. Sun, J. Li, X. Pan, X. Bao, *Sci. Adv.* **2015**, *1*, e1500462.
[64] a) R.-Q. Zou, H. Sakurai, S. Han, R.-Q. Zhong, Q. Xu, *J. Am. Chem. Soc.* **2007**, *129*, 8402; b) A. S. Hoffman, L. M. Debefve, S. Zhang, J. E. Perez-Aguilar, E. T. Conley, K. R. Justl, I. Arslan, D. A. Dixon, B. C. Gates, *ACS Catal.* **2018**, *8*, 3489.
[65] J. Wang, W. Liu, G. Luo, Z. Li, C. Zhao, H. Zhang, M. Zhu, Q. Xu, X. Wang, C. Zhao, Y. Qu, Z. Yang, T. Yao, Y. Li, Y. Lin, Y. Wu, Y. Li, *Energy Environ. Sci.* **2018**, *11*, 3375.
[66] a) X. Zeng, J. Shui, X. Liu, Q. Liu, Y. Li, J. Shang, L. Zheng, R. Yu, *Adv. Energy Mater.* **2018**, *8*, 1701345; b) C. H. Choi, M. Kim, H. C. Kwon, S. J. Cho, S. Yun, H.-T. Kim, K. J. Mayrhofer, H. Kim, M. Choi, *Nat. Commun.* **2016**, *7*, 10922; c) J. Hou, M. Yang, C. Ke, G. Wei, C. Priest, Z. Qiao, G. Wu, J. Zhang, *EnergyChem* **2020**, *2*, 100023.
[67] J. Liu, M. Jiao, B. Mei, Y. Tong, Y. Li, M. Ruan, P. Song, G. Sun, L. Jiang, Y. Wang, Z. Jiang, L. Gu, Z. Zhou, W. Xu, *Angew. Chem., Int. Ed.* **2019**, *58*, 1163.
[68] a) M. Liu, Z. Zhao, X. Duan, Y. Huang, *Adv. Mater.* **2019**, *31*, 1802234; b) X. Huang, Z. Zhao, Y. Chen, E. Zhu, M. Li, X. Duan, Y. Huang, *Energy Environ. Sci.* **2014**, *7*, 2957; c) M. Oezaslan, F. Hasche, P. Strasser, *J. Phys. Chem. Lett.* **2013**, *4*, 3273; d) H. Zhang, M. Jin, Y. Xia, *Chem. Soc. Rev.* **2012**, *41*, 8035; e) C. Zhang, X. Shen, Y. Pan, Z. Peng, *Front. Energy* **2017**, *11*, 268.
[69] a) R. Jiang, L. Li, T. Sheng, G. Hu, Y. Chen, L. Wang, *J. Am. Chem. Soc.* **2018**, *140*, 11594; b) Q. Lai, L. Zheng, Y. Liang, J. He, J. Zhao, J. Chen, *ACS Catal.* **2017**, *7*, 1655; c) Y. Chen, Z. Li, Y. Zhu, D. Sun, X. Liu, L. Xu, Y. Tang, *Adv. Mater.* **2019**, *31*, 1806312.
[70] X. Wan, X. Liu, Y. Li, R. Yu, L. Zheng, W. Yan, H. Wang, M. Xu, J. Shui, *Nat. Catal.* **2019**, *2*, 259.
[71] C. Walling, *Acc. Chem. Res.* **1975**, *8*, 125.
[72] a) P. Song, M. Luo, X. Liu, W. Xing, W. Xu, Z. Jiang, L. Gu, *Adv. Funct. Mater.* **2017**, *27*, 1700802; b) J. Li, S. Chen, N. Yang, M. Deng, S. Ibraheem, J. Deng, J. Li, L. Li, Z. Wei, *Angew. Chem., Int. Ed.* **2019**, *58*, 7035.
[73] a) D. Zhang, W. Chen, Z. Li, Y. Chen, L. Zheng, Y. Gong, Q. Li, R. Shen, Y. Han, W.-C. Cheong, L. Gu, Y. Li, *Chem. Commun.* **2018**, *54*, 4274; b) K. Jiang, P. Wang, S. Guo, X. Zhang, X. Shen, G. Lu, D. Su, X. Huang, *Angew. Chem., Int. Ed.* **2016**, *55*, 9030; c) L. Wei, H. E. Karahan, S. Zhai, H. Liu, X. Chen, Z. Zhou, Y. Lei, Z. Liu, Y. Chen, *Adv. Mater.* **2017**, *29*, 1701410; d) J. Wang, Z. Huang, W. Liu, C. Chang, H. Tang, Z. Li, W. Chen, C. Jia, T. Yao, S. Wei, Y. Wu, Y. Li, *J. Am. Chem. Soc.* **2017**, *139*, 17281.
[74] L. Zhang, J. M. T. A. Fischer, Y. Jia, X. Yan, W. Xu, X. Wang, J. Chen, D. Yang, H. Liu, L. Zhuang, M. Hankel, D. J. Searles, K. Huang, S. Feng, C. L. Brown, X. Yao, *J. Am. Chem. Soc.* **2018**, *140*, 10757.
[75] a) J. Wu, L. Xiong, B. Zhao, M. Liu, L. Huang, *Small Methods* **2020**, *4*, 1900540; b) C. Ling, L. Shi, Y. Ouyang, X. C. Zeng, J. Wang, *Nano Lett.* **2017**, *17*, 5133.
[76] J. Wu, H. Zhou, Q. Li, M. Chen, J. Wan, N. Zhang, L. Xiong, S. Li, B. Y. Xia, G. Feng, M. Liu, L. Huang, *Adv. Energy Mater.* **2019**, *9*, 1900149.
[77] H. Fei, J. Dong, Y. Feng, C. S. Allen, C. Wan, B. Volosskiy, M. Li, Z. Zhao, Y. Wang, H. Sun, P. An, W. Chen, Z. Guo, C. Lee, D. Chen, I. Shakir, M. Liu, T. Hu, Y. Li, A. I. Kirkland, X. Duan, Y. Huang, *Nat. Catal.* **2018**, *1*, 63.
[78] Y. Yao, S. Hu, W. Chen, Z.-Q. Huang, W. Wei, T. Yao, R. Liu, K. Zang, X. Wang, G. Wu, W. Yuan, T. Yuan, B. Zhu, W. Liu, Z. Li, D. He, Z. Xue, Y. Wang, X. Zheng, J. Dong, C.-R. Chang, Y. Chen, X. Hong, J. Luo, S. Wei, W.-X. Li, P. Strasser, Y. Wu, Y. Li, *Nat. Catal.* **2019**, *2*, 304.
[79] Y. Zheng, Y. Jiao, A. Vasileff, S. Z. Qiao, *Angew. Chem., Int. Ed.* **2018**, *57*, 7568.
[80] a) S. Ye, F. Luo, Q. Zhang, P. Zhang, T. Xu, Q. Wang, D. He, L. Guo, Y. Zhang, C. He, X. Ouyang, M. Gu, J. Liu, X. Sun, *Energy Environ. Sci.* **2019**, *12*, 1000; b) H. Zhang, P. An, W. Zhou, B. Y. Guan, P. Zhang, J. Dong, X. W. D. Lou, *Sci. Adv.* **2018**, *4*, eaao6657; c) X. P. Yin, H. J. Wang, S. F. Tang, X. L. Lu, M. Shu, R. Si, T. B. Lu, *Angew. Chem., Int. Ed.* **2018**, *57*, 9382.
[81] a) H. J. Qiu, Y. Ito, W. Cong, Y. Tan, P. Liu, A. Hirata, T. Fujita, Z. Tang, M. Chen, *Angew. Chem., Int. Ed.* **2015**, *54*, 14031; b) L. Cao, Q. Luo, W. Liu, Y. Lin, X. Liu, Y. Cao, W. Zhang, Y. Wu, J. Yang, T. Yao, S. Wei, *Nat. Catal.* **2019**, *2*, 134.
[82] L. Zhang, Y. Jia, G. Gao, X. Yan, N. Chen, J. Chen, M. T. Soo, B. Wood, D. Yang, A. Du, X. Yao, *Chem* **2018**, *4*, 285.
[83] J. Wan, Z. Zhao, H. Shang, B. Peng, W. Chen, J. Pei, L. Zheng, J. Dong, R. Cao, R. Sarangi, Z. Jiang, D. Zhou, Z. Zhuang, J. Zhang, D. Wang, Y. Li, *J. Am. Chem. Soc.* **2020**, *142*, 8431.
[84] C. Yan, H. Li, Y. Ye, H. Wu, F. Cai, R. Si, J. Xiao, S. Miao, S. Xie, F. Yang, Y. Li, G. Wang, X. Bao, *Energy Environ. Sci.* **2018**, *11*, 1204.
[85] Y. Pan, R. Lin, Y. Chen, S. Liu, W. Zhu, X. Cao, W. Chen, K. Wu, W.-C. Cheong, Y. Wang, L. Zheng, J. Luo, Y. Lin, Y. Liu, C. Liu, J. Li, Q. Lu, X. Chen, D. Wang, Q. Peng, C. Chen, Y. Li, *J. Am. Chem. Soc.* **2018**, *140*, 4218.
[86] F. Pan, H. Zhang, K. Liu, D. Cullen, K. More, M. Wang, Z. Feng, G. Wang, G. Wu, Y. Li, *ACS Catal.* **2018**, *8*, 3116.
[87] W. Ren, X. Tan, W. Yang, C. Jia, S. Xu, K. Wang, S. C. Smith, C. Zhao, *Angew. Chem., Int. Ed.* **2019**, *58*, 6972.
[88] a) J. Albo, M. Alvarez-Guerra, P. Castaño, A. Irabien, *Green Chem.* **2015**, *17*, 2304; b) J. Albo, A. Irabien, *J. Catal.* **2016**, *343*, 232.
[89] C. Genovese, M. E. Schuster, E. K. Gibson, D. Gianolio, V. Posligua, R. Grau-Crespo, G. Cibin, P. P. Wells, D. Garai, V. Solokha, S. Krick Calderon, J. J. Velasco-Velez, C. Ampelli, S. Perathoner, G. Held, G. Centi, R. Arrigo, *Nat. Commun.* **2018**, *9*, 935.
[90] S. Gao, Y. Lin, X. Jiao, Y. Sun, Q. Luo, W. Zhang, D. Li, J. Yang, Y. Xie, *Nature* **2016**, *529*, 68.
[91] Z. Zhao, G. Lu, *J. Phys. Chem. C* **2019**, *123*, 4380.
[92] R. Zhao, H. Xie, L. Chang, X. Zhang, X. Zhu, X. Tong, T. Wang, Y. Luo, P. Wei, Z. Wang, X. Sun, *EnergyChem* **2019**, *1*, 100011.

[93] a) C. J. Van der Ham, M. T. Koper, D. G. Hetterscheid, *Chem. Soc. Rev.* **2014**, *43*, 5183; b) Y. Wan, J. Xu, R. Lv, *Mater. Today* **2019**, *27*, 69.
[94] a) Y. Luo, G.-F. Chen, L. Ding, X. Chen, L.-X. Ding, H. Wang, *Joule* **2019**, *3*, 279; b) W. Qiu, X.-Y. Xie, J. Qiu, W.-H. Fang, R. Liang, X. Ren, X. Ji, G. Cui, A. M. Asiri, G. Cui, B. Tang, X. Sun, *Nat. Commun.* **2018**, *9*, 3485; c) J. Zhao, Z. Chen, *J. Am. Chem. Soc.* **2017**, *139*, 12480; d) Y. Liu, Y. Su, X. Quan, X. Fan, S. Chen, H. Yu, H. Zhao, Y. Zhang, J. Zhao, *ACS Catal.* **2018**, *8*, 1186.
[95] a) X. Wang, W. Wang, M. Qiao, G. Wu, W. Chen, T. Yuan, Q. Xu, M. Chen, Y. Zhang, X. Wang, J. Wang, J. Ge, X. Hong, Y. Li, Y. Wu, Y. Li, *Sci. Bull.* **2018**, *63*, 1246; b) Z. Geng, Y. Liu, X. Kong, P. Li, K. Li, Z. Liu, J. Du, M. Shu, R. Si, J. Zeng, *Adv. Mater.* **2018**, *30*, 1803498; c) H. Tao, C. Choi, L.-X. Ding, Z. Jiang, Z. Han, M. Jia, Q. Fan, Y. Gao, H. Wang, A. W. Robertson, S. Hong, Y. Jung, S. Liu, Z. Sun, *Chem* **2019**, *5*, 204; d) C. He, Z.-Y. Wu, L. Zhao, M. Ming, Y. Zhang, Y. Yi, J.-S. Hu, *ACS Catal.* **2019**, *9*, 7311; e) F. Lü, S. Zhao, R. Guo, J. He, X. Peng, H. Bao, J. Fu, L. Han, G. Qi, J. Luo, X. Tang, X. Liu, *Nano Energy* **2019**, *61*, 420; f) L. Han, X. Liu, J. Chen, R. Lin, H. Liu, F. Lü, S. Bak, Z. Liang, S. Zhao, E. Stavitski, J. Luo, R. R. Adzic, H. L. Xin, *Angew. Chem., Int. Ed.* **2019**, *58*, 2321.
[96] a) X. Sun, A. I. Olivos-Suarez, D. Osadchii, M. J. V. Romero, F. Kapteijn, J. Gascon, *J. Catal.* **2018**, *357*, 20; b) S. Wei, A. Li, J.-C. Liu, Z. Li, W. Chen, Y. Gong, Q. Zhang, W.-C. Cheong, Y. Wang, L. Zheng, H. Xiao, C. Chen, D. Wang, Q. Peng, L. Gu, X. Han, J. Li, Y. Li, *Nat. Nanotechnol.* **2018**, *13*, 856.

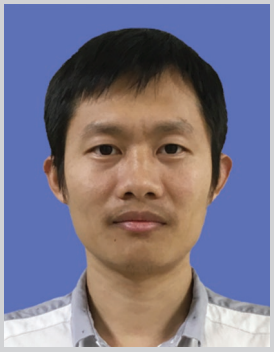

Lianli Zou received his Ph.D. in 2019 from Kobe University under the supervision of Prof. Qiang Xu. He is now working as a postdoctoral researcher in AIST-Kyoto University Chemical Energy Materials Open Innovation Laboratory (ChEM-OIL). His research interests are focusing on the synthesis and application of MOF-derived nanomaterials for catalysis and energy storage.

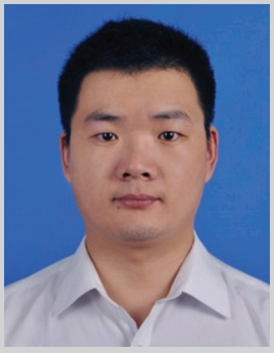

Yong-Sheng Wei obtained his Ph.D. in 2015 from Sun Yat-Sen University under the supervision of Prof. Xiao-Ming Chen and Prof. Jie-Peng Zhang. He currently works as a postdoctoral fellow with Prof. Qiang Xu at AIST-Kyoto University Chemical Energy Materials Open Innovation Laboratory (ChEM-OIL), where he is working on nanostructured materials for catalysis and energy.

Qiang Xu received his Ph.D. in Physical Chemistry from Osaka University in 1994. He is director of AIST-Kyoto University ChEM-OIL and specially-appointed professor of Yangzhou University. His research interests include the chemistry of nanomaterials and their applications, especially for catalysis and energy. He is a fellow of the Engineering Academy of Japan (EAJ), the European Academy of Sciences (EURASC), and the National Academy of Sciences, India (NASI).